A Two-Tier Magnetic Material Strategy for Metric Engineering: From the Rare-Earth-Free $(\mathrm{Fe}_{0.92}\mathrm{Co}_{0.08})_2(\mathrm{P}_{0.78}\mathrm{Si}_{0.22})$ Gap Magnet to the HeliFe-MADA Architecture for the GU-RVG Framework

Jesse D. Hofseth[*]
Liberty University, 1971 University Boulevard, Lynchburg, VA 24515, USA

Eric R. Weinstein[†]

(Dated: May 4, 2026)

The realization of the Geometric Unity–Refractive Vacuum Gravity (GU-RVG) synthesis as a deployable aerospace technology is bounded fundamentally by materials science. The recursive Magnetic Amplification and Direction Assembly (MADA) demands a physical substrate capable of sustaining absolute South-South (or North-North) pole opposition across a comparatively wide central gap and forcing the resulting frustrated flux across 10–100 μm micro-gaps within a targeted laminated magnetic-circuit wall, where 0.15–0.35 mm laminations separated by micron-scale dielectric interlayers generate microscopic gradient singularities in $\nabla(\boldsymbol{B}\cdot\boldsymbol{B})$. These singularities trigger dilaton condensation and couple the boundary helicity to the topological Chern-Simons terms of the 14-dimensional Observerse Y^{14} [1, 2, 5]. In a deployed airframe, multiple MADA arrays are AI-controlled and mechanically gimbaled within large, heavy spherical, discoidal, or cylindrical laminated magnetic circuits; the net thrust vector is directed antiparallel to the vector sum of the array-targeted points on the interior wall of the surrounding magnetic circuit, and the propulsive force is the macroscopic integral of the microscopic $\nabla(\boldsymbol{B}\cdot\boldsymbol{B})$ singularities developed within the circuit's targeted laminations. The Scalar-Hydraulic Drive (SHD) and the Asymmetric Dilaton Pump Generator (ADPG) both employ *partially-hybridized* MADA arrays—permanent-magnet cores augmented by embedded pulsing coils and servo-driven flux-shunting irises—differing not in their underlying MADA topology but in which asymmetry, spatial or temporal, primarily drives the metric coupling and in whether the unit is configured for propulsion or stationary energy extraction [2, 6, 7]. Conventional materials fail along two physically distinct roles. As candidate *magnetic materials*—the hard, permanent-magnet substrate—neodymium-iron-boron ($\mathrm{Nd}_2\mathrm{Fe}_{14}\mathrm{B}$) is geopolitically constrained [6, 46] and metastable α''-$\mathrm{Fe}_{16}\mathrm{N}_2$ decomposes above 250°C [50, 54, 56]. As candidate *magnetic-circuit materials*—the soft, high-permeability return-yoke and flux-shunting-iris substrate—commercial Hiperco-50 (Fe-49Co-2V) is thermally robust but limited to $J_s \approx 2.4$ T [47, 48], and Minnealloy, the soft Fe-N-family alloy chemically related to but functionally distinct from α''-$\mathrm{Fe}_{16}\mathrm{N}_2$, shares the same $< 250^\circ$C metastability ceiling [55]. We propose a complementary two-tier material strategy in which the differentiator is *material cost and manufacturing difficulty*, not subsystem function: both tiers are valid in both SHD and ADPG hardware, and the choice between them is determined by deployment context and economics. **Tier I** is the rare-earth-free iron-phosphide alloy $(\mathrm{Fe}_{0.92}\mathrm{Co}_{0.08})_2(\mathrm{P}_{0.78}\mathrm{Si}_{0.22})$, supplemented by 0.5–2.0 at.% trace pinning additions of manganese or aluminum. Cobalt site substitution lifts the Curie temperature beyond 500 K, silicon doping maximizes the uniaxial magnetocrystalline anisotropy to $K_1 \approx 1.09$ MJ/m^3 and suppresses the first-order magnetoelastic transition of binary $\mathrm{Fe}_2\mathrm{P}$, and high-energy ball milling followed by Spark Plasma Sintering produces sub-micron core-shell grains with intrinsic coercivity $H_{cj} = 5$–12 kOe and energy product $(BH)_{\max} \approx 180$ kJ/m^3 (≈ 22.6 MGOe). *Tier I addresses only the magnetic-material role*; Tier I airframes pair the $(\mathrm{Fe}_{0.92}\mathrm{Co}_{0.08})_2(\mathrm{P}_{0.78}\mathrm{Si}_{0.22})$ pole magnets with a separate soft-yoke substrate—typically Hiperco-50—to complete the MADA flux circuit. Tier I is intended for global civilian and commercial deployment—"everyone on Earth"—in mass-produced MADA arrays where the volumetric cost-per-magnet must be bounded by commodity rock-forming elements. **Tier II** is the HeliFe-MADA architecture, a chirally-doped, interstitially-nitrogenated ThMn_{12}-type exchange-spring nanocomposite of nominal stoichiometry $\mathrm{Nd}_{0.05}(\mathrm{Fe}_{0.68}\mathrm{Co}_{0.17}\mathrm{V}_{0.05})_{11.5}\mathrm{N}_{0.05}$ with trace Pt/Ir/Mn, which transcends the Slater-Pauling barrier through the magnetovolume effect to reach $J_s \approx 2.7$ T while intrinsically generating macroscopic magnetic helicity $H_m \neq 0$ via engineered Dzyaloshinskii-Moriya interactions, with theoretical $(BH)_{\max}$ approaching 1450 kJ/m^3 (~ 182 MGOe). Tier II is fabricated by magnetic field-assisted laser powder-bed fusion (MF-L-PBF) with monolithic ceramic interlayer lamination and post-consolidation inductively-coupled-plasma nitrogenation, yielding functionally-graded soft-yoke/hard-pole geometries. *Tier II addresses both roles within a single monolithic build*: the same MF-L-PBF process produces the hard nitrogenated ThMn_{12} pole tips (magnetic-material role) and the coarsened soft bcc Fe-Co return yokes (magnetic-circuit-material role), eliminating the dissimilar-material joint required of Tier I airframes. This premium tier is intended for exquisite military and intelligence platforms and for high-end consumer applications where saturation, intrinsic chirality, and pulsed-burst tolerance must be maximized regardless of unit cost. The Master Equation of Levitation $\boldsymbol{F}_{\text{lift}} = \int_V (1/2\mu_0)\, \Theta_{\text{dilaton}}(B)\, \nabla(\boldsymbol{B}\cdot\boldsymbol{B})\, dV$ is satisfied by either tier; together they span the full economic-deployment spectrum of the GU-RVG hardware program.

Keywords: Geometric Unity, Refractive Vacuum Gravity, Metric Engineering, MADA, Iron Phosphide, Fe_2P, $ThMn_{12}$, HeliFe-MADA, Slater-Pauling Barrier, Magnetovolume Effect, Dzyaloshinskii-Moriya Interaction, Magnetic Helicity, Skyrmions, Exchange-Spring Magnet, Magnetocrystalline Anisotropy, Coercivity, Permanent Magnets, Rare-Earth-Free, Scalar-Hydraulic Drive, ADPG, 95 GeV Dilaton, Trace Anomaly, Sub-Micron Grain, Spark Plasma Sintering, Magnetic Field-Assisted Additive Manufacturing, Plasma Nitrogenation, Gap Magnet

Published in: General Science Journal (May 4, 2026).
Available online at: gsjournal.net/.../View/10536
Archived version (final PDF): Zenodo.
DOI: 10.5281/zenodo.20031790

I. INTRODUCTION TO THE MATERIALS SCIENCE OF METRIC ENGINEERING

The historical trajectory of fundamental physics and aerospace engineering has long been constrained by a profound methodological schism. On one side of the epistemological divide lies the pursuit of top-down geometric unification, operating at the highest conceivable energy scales to derive the constituents of reality from pure topology, higher-dimensional manifolds, and geometric phases [1, 2]. On the other lies the pragmatic pursuit of phenomenological effective field theories and applied materials science, focused on observable parameters and the physical manipulation of matter [5, 30]. The synthesis of Geometric Unity (GU) and Refractive Vacuum Gravity (RVG) resolves this dichotomy by establishing a framework in which the spacetime metric is engineered at macroscopic, observable scales using solid-state electromagnetic architectures [2, 3]. The synthesis treats the physical vacuum not as an empty mathematical void, but as an active, refractive fluid whose dielectric permittivity and magnetic permeability are dynamically modulated by a scalar field coupled directly to the trace anomaly of the energy-momentum tensor [23, 26, 27].

The physical actualization of this metric engineering rests most efficiently upon the Magnetic Amplification and Direction Assembly (MADA) [6, 45]. The MADA core operates as a macroscopic geometric reactor, designed to generate extreme spatial gradients of $\boldsymbol{B} \cdot \boldsymbol{B}$. By forcing magnetic flux lines into highly confined topological configurations, the assembly produces a spatial singularity in magnetic field intensity, extracting usable mechanical work from the scalar vacuum condensate. In a deployed airframe, multiple MADA arrays are AI-controlled and mechanically gimbaled within large, heavy spherical, discoidal, or cylindrical laminated magnetic circuits; the net thrust vector is antiparallel to the vector sum of the points on the interior wall of the surrounding magnetic circuit at which the constituent arrays are momentarily targeted. Realization of the architecture has, however, been persistently obstructed by a severe materials-science bottleneck. The hardware must survive absolute pole opposition—specifically South-South (or North-North) opposition across a wide central gap, driving the combined flux across 10–100 μm micro-gaps in a targeted laminated magnetic-circuit wall, where the micron-scale dielectric gaps between 0.15–0.35 mm laminations trap and concentrate the flux—without undergoing avalanche demagnetization, while simultaneously projecting—in the case of 12 magnets per position, 60 magnets per MADA, and 300 magnets per MADA array—a per-MADA-array virtual magnetic emission equivalent to 203–540 T toward the targeted lamination region (Regime 2 of the three-regime pressure budget formalized in Sec. V A) [2, 6].

No conventional candidate satisfies the requirements of the partially-hybridized MADA array along its two physically distinct material roles—the hard, permanent-magnet substrate (*magnetic-material role*) and the soft, high-permeability return-yoke and flux-shunting-iris substrate (*magnetic-circuit-material role*). For the magnetic-material role: while neodymium-iron-boron ($Nd_2Fe_{14}B$) offers high remanence, it is constrained by severe supply-chain vulnerabilities, geopolitical monopolization, and prohibitive environmental costs [6, 46]; the rare-earth-free theoretical ideal, metastable α''-$Fe_{16}N_2$, suffers catastrophic thermodynamic phase instability above 250°C [50, 54, 56]. For the magnetic-circuit-material role: commercial iron-cobalt-vanadium alloys such as Hiperco-50 provide excellent thermal stability and high μ_r but cap at $J_s \approx$ 2.4 T [47, 48]; the chemically related Minnealloy soft alloys reach ~ 2.9 T but inherit the same <250°C metastability ceiling that disqualifies α''-$Fe_{16}N_2$ from sustained ADPG service [54, 55].

The present work provides a definitive analysis of two complementary magnetic-material tiers required to bridge this engineering gap. The differentiator between them is *material cost and manufacturing difficulty*, not subsystem function. Both the Scalar-Hydraulic Drive (SHD) and the Asymmetric Dilaton Pump Generator (ADPG) employ partially-hybridized MADA arrays [2, 6, 7]; both can be populated with either tier of magnetic material. The choice between tiers is therefore an economic and deployment-context decision rather than a physics constraint.

Tier I is the rare-earth-free iron-phosphide alloy $(Fe_{0.92}Co_{0.08})_2(P_{0.78}Si_{0.22})$, supplemented by minor trace

---

[*] jdhofseth@liberty.edu; ORCiD: 0009-0005-5370-1112

[†] Passive authorship attribution: originator of the Geometric Unity (GU) framework, which provides the geometric foundation for the present materials-science synthesis. The specific integration with Refractive Vacuum Gravity, the iron-phosphide and HeliFe-MADA alloy specifications, and any errors of derivation that follow are the sole responsibility of the active author.

additions of grain-boundary pinning elements such as manganese or aluminum [57]. Tier I addresses only the magnetic-material role; a Tier I airframe pairs the $(\mathrm{Fe}_{0.92}\mathrm{Co}_{0.08})_2(\mathrm{P}_{0.78}\mathrm{Si}_{0.22})$ pole magnets with a separate soft-yoke substrate—typically Hiperco-50—to complete the MADA flux circuit. Tier I is intended for global civilian and commercial deployment—"everyone on Earth"—in mass-produced MADA arrays where commodity availability, geopolitical resilience, and low unit cost are paramount.

Tier II is the HeliFe-MADA architecture [77–79], a chirally-doped, interstitially-nitrogenated ThMn_{12}-type exchange-spring nanocomposite engineered to break the Slater-Pauling barrier ($J_s \approx 2.7$ T) while spontaneously generating macroscopic magnetic helicity through engineered Dzyaloshinskii-Moriya interactions [82, 83]. Tier II addresses both material roles simultaneously through its functionally-graded exchange-spring architecture: the same MF-L-PBF process produces the hard nitrogenated ThMn_{12} pole tips (magnetic-material role) and the coarsened soft bcc Fe-Co return yokes (magnetic-circuit-material role) within a single monolithic build, eliminating the dissimilar-material joint required of Tier I airframes. Tier II is intended for exquisite military and intelligence platforms and for high-end consumer applications, where saturation, intrinsic chirality, and pulsed-burst tolerance must be maximized regardless of unit cost.

By systematically deconstructing the crystallography, thermodynamic stability, microstructural engineering, and quantum-mechanical interactions of both materials, the analysis demonstrates how this two-tier strategy serves as the indispensable physical interface required to ground the holographic projections of the 14-dimensional Observerse Y^{14} into an engineerable propulsion program that scales from civilian fleet aviation to exquisite black-program hardware [2, 3]. The complete cost-versus-performance topology of the strategy is summarized in Fig. 1.

II. THE THEORETICAL ARCHITECTURE OF THE GU-RVG FRAMEWORK

To understand the extreme physical constraints placed upon the magnetic core material, the underlying theoretical physics of the GU-RVG synthesis must be rigorously established. The framework posits that the observable 4-dimensional spacetime (X^4) is not a fundamental, immutable entity but rather a holographic boundary screen upon which the dynamics of a massive 14-dimensional bulk manifold—the Observerse, Y^{14}—are projected [1, 3, 14, 15].

A. The 14-Dimensional Observerse and the Thermodynamic Heat Sink

A primary obstacle in aerospace metric engineering is the thermodynamic paradox associated with localized metric deformation. Modifying the spacetime metric to create a propulsive gradient—of the Alcubierre-type warp-bubble class [32]—requires substantial shifts in entropy. Were this entropy strictly confined to a standard 4-dimensional pseudo-Riemannian manifold, the resulting thermal release would incinerate the vessel and its surroundings. The GU-RVG synthesis circumvents the paradox by treating the ten hidden dimensions of the Observerse as a macroscopic, higher-dimensional thermodynamic heat sink [2, 3].

The mathematical bridge connecting the 14-dimensional bulk to the 4-dimensional boundary is established through the chimeric bundle, defined as the direct sum of the vertical sub-bundle V along the fibers and the horizontal sub-bundle H^* pulled back from the tangent space of the boundary:

$$C(Y) = V \oplus H^*. \tag{1}$$

The refractive index of the vacuum is formally identified as a direct physical measure of the local volume of the fibers in this bundle [1, 3]. When the physical MADA hardware pumps the vacuum with intense magnetic gradients, it transfers immense entropy from the electromagnetic sector on the 4-dimensional slice into the geometric transverse degrees of freedom of the hidden dimensions. The capacity of the bulk to absorb this entropy scales with the compactification length, $S_{\text{bulk}} \sim (L_{\text{extra}}/\ell_p)^{10}$, ensuring that local usable work is extracted on the boundary while global entropy strictly increases, in compliance with the second law of thermodynamics.

The translation of boundary observables into bulk geometry is governed by the Zorro construction, a bidirectional data flow linking metrics to connections across the dimensional divide [1]. A choice of metric $\gimel$ on the boundary induces a Levi-Civita connection $\aleph_\gimel$, which in turn determines a metric $g_\aleph$ on the bulk, ultimately fixing a spin connection on the structure bundle of Dirac spinors. This sequence is the geometric generator of the Hamilton-Kabat-Lifschytz-Lowe (HKLL) bulk-reconstruction smearing kernel [16, 17], demonstrating that intense magnetic observation on the 4-dimensional slice rigorously fixes the geometry of the 14-dimensional bulk.

The introduction of this high-energy bulk structure requires the resolution of mathematical anomalies that previously plagued unification theories [8]. The mapping from the real Clifford algebra $\mathrm{Cl}_{14}(\mathbb{R})$ to the Lie algebra of skew-Hermitian matrices $\mathfrak{u}(128)$ is a non-isomorphism over the real numbers; furthermore, the use of the positive-definite unitary gauge group $U(128)$ induces a fatal abelian chiral anomaly because the eighth Chern-class expansion evaluates to a non-zero coefficient owing to the central $U(1)$ trace [18, 19]. The framework resolves this through strict complexification of the underlying algebra to $\mathrm{Cl}_{14}(\mathbb{C})$ and

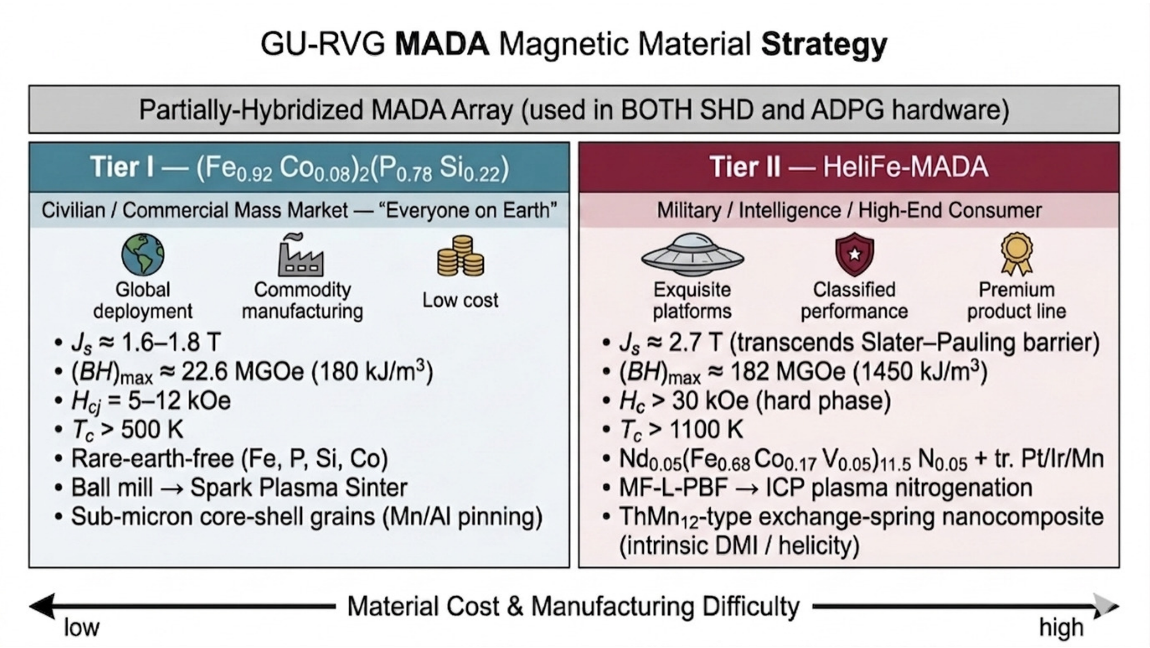

FIG. 1. The two-tier magnetic-material strategy for GU-RVG metric engineering. Both Tier I ($(\mathrm{Fe}_{0.92}\mathrm{Co}_{0.08})_2(\mathrm{P}_{0.78}\mathrm{Si}_{0.22})$) and Tier II (HeliFe-mada) populate the *same* partially-hybridized mada arrays in either shd or adpg hardware; the differentiator is *material cost and manufacturing difficulty*, not subsystem function. Tier I targets global civilian and commercial deployment via commodity supply chains and mature powder metallurgy ($J_s \approx 1.6$–1.8 T, $(BH)_{\max} \approx 22.6$ MGOe). Tier II targets exquisite military, intelligence, and high-end consumer platforms via premium magnetic field-assisted additive manufacturing and ICP plasma nitrogenation ($J_s \approx 2.7$ T, $(BH)_{\max} \approx 182$ MGOe), transcending the Slater-Pauling barrier through the magnetovolume effect.

the subsequent migration of the gauge group to the mixed-signature non-compact unitary representation $U(64, 64)$, which naturally accommodates the $(7, 7)$ split signature of the Observerse [1, 3]. By projecting out the central trace component, the anomaly polynomial I_{16} vanishes for the semi-simple quotient $SU(64, 64)$. Any residual gravitational or mixed anomalies are canceled by a 14-dimensional Green-Schwarz mechanism [18], ensuring that the entire Observerse bulk-to-boundary projection remains mathematically consistent and anomaly-free.

B. The 95.4 GeV Dilaton and Conformal Symmetry Breaking

The mechanism by which the magnetic material interfaces with the 14-dimensional geometry is mediated by a specific scalar field. The framework identifies the 95.4 GeV resonance—the persistent diphoton and $b\bar{b}$ excess observed by the CMS and ATLAS collaborations at the Large Hadron Collider with a combined local significance of 3.1σ [9–11]—as the physical manifestation of the dilaton, a pseudo-Goldstone boson associated with the spontaneous breaking of conformal scale invariance [12, 13].

The existence and coupling strength of this dilaton are corroborated by the topological generation of lepton masses [4, 35, 36]. In the GU-RVG framework, the mass hierarchy of charged fermions is fixed by the topological winding structure of the S^5 compactification manifold. There exist exactly three stable fundamental hyperstalk winding topologies, corresponding to the three generations of charged leptons. The $SO(6)$ isometry breaks spontaneously to an $S_3 \times U(1)$ symmetry, yielding a democratic mass matrix whose Frobenius norm identity forces the inverse participation ratio of the square-root mass distribution to equal exactly 2/3:

$$Q_\ell \equiv \frac{m_e + m_\mu + m_\tau}{(\sqrt{m_e} + \sqrt{m_\mu} + \sqrt{m_\tau})^2} = \frac{2}{3}. \tag{2}$$

Empirical high-precision CODATA and Particle Data Group values [38, 39] reveal that the actual Koide parameter is $Q_\ell^{\mathrm{exp}} = 0.66666050$, a 9.25 ppm deviation from the exact 2/3 geometric ideal. The framework identifies this deviation as the quantifiable phenomenological footprint of the dilaton field acquiring a vacuum expectation value and shifting the mass matrix via 1-loop radiative corrections [4, 37]. Mathematically modeling this "Geometric g-2" shift isolates the dilaton decay constant at $f_\phi \approx 27.2$ TeV, providing the fundamental anchor for all subsequent metric-engineering calculations.

III. DISFORMAL QED AND THE MASTER EQUATION OF LEVITATION

Unlike the Standard Model Higgs boson, which couples proportionally to fermion mass via Yukawa interactions to generate inertia, the dilaton couples directly and exclusively to the trace of the energy-momentum tensor [5, 23]. In classical electrodynamics the energy-momentum tensor of the electromagnetic field is strictly traceless. Quantum effects—specifically the renormalization of the electric charge—induce a trace anomaly [21, 22]:

$$T^{\mu}_{\ \mu} = \frac{\beta(g)}{2g} F_{\mu\nu}F^{\mu\nu} + m_f \bar{\psi}\psi. \tag{3}$$

The presence of this quantum trace anomaly permits an interaction between the electromagnetic field generated by the MADA core and the scalar dilaton field [2, 5].

A. The Magnetic-Dominance Imperative

The interaction Lagrangian density governing this relationship is [5]

$$\mathcal{L}_{\text{int}} = \frac{\phi}{f_\phi} \left[\frac{\beta(g)}{2g} F_{\mu\nu}F^{\mu\nu} + m_f \bar{\psi}\psi \right], \tag{4}$$

in which $F_{\mu\nu}F^{\mu\nu} \propto B^2 - E^2$. This establishes the absolute design imperative for the physical hardware. Because the coupling is proportional to $B^2 - E^2$, the scalar field can be sourced effectively only when the magnetic energy density vastly exceeds the electric energy density within the active operational zone. Electric fields are fundamentally screened by vacuum polarization up to the Schwinger limit [21, 29] and are therefore highly inefficient for metric engineering; magnetic fields, by contrast, can be geometrically stacked to extreme densities without spontaneous breakdown.

B. The Gordon Optical Metric and Vacuum Buoyancy

Under extreme magnetic stress, the local vacuum transitions from a stiff linear regime into a soft non-linear regime [22, 28]. The physical metric is modified by the scalar dilaton field through a disformal transformation [26, 27]: a conformal factor rescales the volume element isotropically, while a critical disformal term distorts the metric anisotropically along the direction of the scalar gradient. In the optical limit this disformal transformation reduces to the Gordon optical metric [24, 25], which dictates the effective spacetime geometry experienced by photons and matter propagating through a refractive medium.

The vacuum refractive index $K(\boldsymbol{x})$ is modeled as a non-linear perturbation from the vacuum ground state, modulated by the dimensionless dilaton coupling at the 95.4 GeV scale and by the ratio of the applied magnetic field to a critical threshold field. When the refractive index is driven above unity, the effective optical path length increases, establishing a gravitational potential directly isomorphic to the refractive gradient [30, 31]. The geometric mechanism by which the magnetic-material core sources this refractive perturbation is illustrated in Fig. 2.

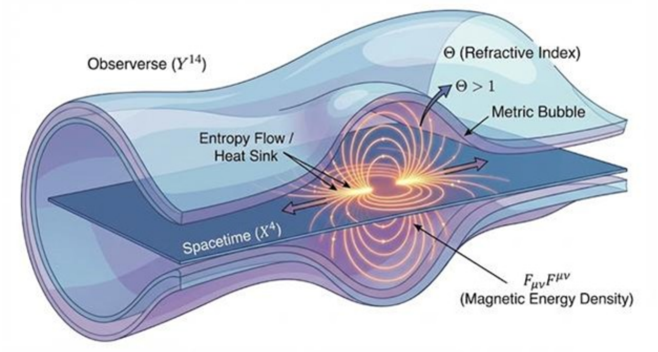

FIG. 2. The geometric mechanism of Refractive Vacuum Gravity. The 14-dimensional Observerse (Y^{14}) acts as a thermodynamic heat sink. The scalar field Θ (refractive index) couples to the electromagnetic invariant $F_{\mu\nu}F^{\mu\nu}$ via the trace anomaly, allowing the "metric bubble" to be inflated by high-density magnetic fields generated by either Tier I or Tier II MADA arrays.

The macroscopic propulsive force extractable from this refractive vacuum is formalized in the Master Equation of Levitation. Derived from the classical Helmholtz force density on a dielectric medium in a charge-neutral, magnetically dominant region, the force density is governed strictly by the gradient terms. Integrating over the active volume of the magnetic core yields

$$\boldsymbol{F}_{\text{lift}} = \int_V \left(\frac{1}{2\mu_0}\, \Theta_{\text{dilaton}}(B)\, \nabla(\boldsymbol{B}\cdot\boldsymbol{B}) \right) dV. \tag{5}$$

This derivation imposes two absolute physical requirements on the magnetic material. First, the material must sustain high absolute field intensities to reach the non-linear supra-saturation regime that activates the dilaton enhancement factor $\Theta_{\text{dilaton}}(B)$. Second, because a perfectly uniform field has spatial gradient zero and therefore generates no propulsive force, the material must be structured into geometries capable of generating severe spatial micro-singularities. The negative sign of the vacuum force density ensures that the net force pushes the physical system away from regions of highest magnetic energy density, establishing the phenomenon of vacuum buoyancy [6, 33].

IV. THE TOPOLOGICAL EFFICIENCY OF THE MADA ARCHITECTURE

To meet the stringent geometric requirements of Eq. (5), standard solenoids, Halbach arrays, and simple dipole configurations are entirely inadequate. The framework underscores the efficiency of the recursive Magnetic Amplification and Direction Assembly (MADA) [6, 45], the canonical multi-unit array topology of which is shown in Fig. 3.

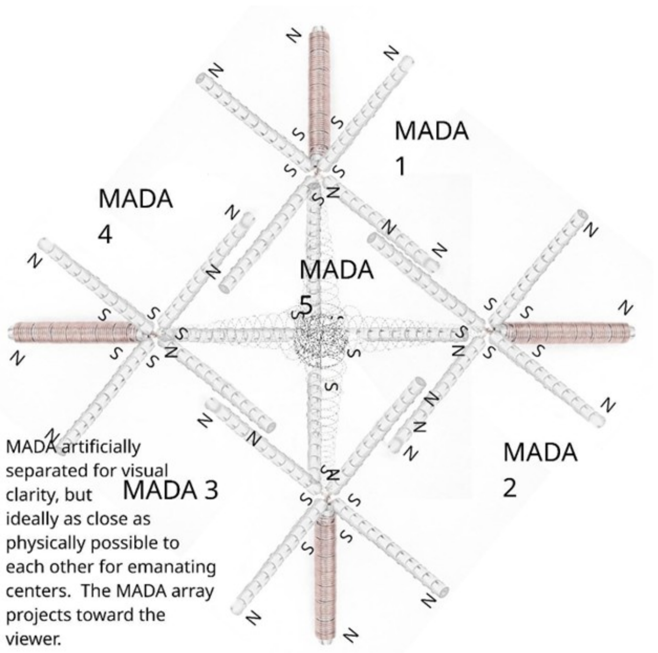

MADA artificially separated for visual clarity, but ideally as close as physically possible to each other for emanating centers. The MADA array projects toward the viewer.

FIG. 3. Five-MADA distributed array configuration (units separated for visual clarity). Each 60-magnet partially-hybridized MADA replaces a single magnet of the original Bushman patent geometry: one unopposed MADA on the beam axis (X) and two opposing pairs on the Y and Z axes, with all South (or North) poles converging at a common center to form the frustrated focusing zone. All three axes are mutually perpendicular in the physical assembly; the oblique angles in the figure are an artifact of the isometric projection. The initial gap between the five opposing MADA units constituting one MADA array is at least as large as a single constituent magnet; the propulsive $\nabla(\boldsymbol{B} \cdot \boldsymbol{B})$ singularity is therefore not borne in this central array-internal separation but rather develops where the combined, frustrated flux is forced across the 10–100 μm micro-gaps within the targeted laminated magnetic-circuit wall, in which 0.15–0.35 mm laminations and micron-scale dielectric gaps generate the gradient micro-singularities (Regime 3 of the pressure budget, Sec. V A). With 12 magnets per MADA position and 5 positions per MADA, each MADA contains 60 magnets and each five-MADA array contains 300 high-power magnets, projecting a virtual $B_{\text{opposing}} \approx 203$–$540$ T linear-superposition emission toward the targeted lamination region (Regime 2 of the pressure budget); the actual macroscopic field delivered to the wall surface is attenuated by geometric dispersion of the order of 10–25%, in keeping with the figurative magnetic-laser analogy rather than with coherent optical focusing. Within the array itself, the four non-rear MADA modules face one another in opposing pairs at gap $d \gtrsim L_{\text{magnet}}$, with each MADA emitting an individual virtual $B_0 \approx 40.6$–108 T; (Caption continued in next column).

FIG. 3. (Continued.) the resulting near-field reciprocal Maxwell stress on the constituent magnets is Regime 1 of the pressure budget. Stacking multiple such arrays multiplies the Regime 2 wall projection proportionally—two or three full arrays deliver two or three times the array-wise virtual pressure—enabling the extreme regimes discussed in Sec. IX. The same array topology is populated with either Tier I ($(\mathrm{Fe}_{0.92}\mathrm{Co}_{0.08})_2(\mathrm{P}_{0.78}\mathrm{Si}_{0.22})$) gap magnets or the functionally-graded Tier II (HeliFe-MADA) architecture according to deployment context; in the Tier II case, the in-situ deposition of micro-layers of electrically insulating ceramic during the monolithic build effectively laminates the soft yokes themselves, suppressing eddy-current losses under pulsed excitation far below the level achievable with conventional stacked-sheet cores such as Hiperco-50.

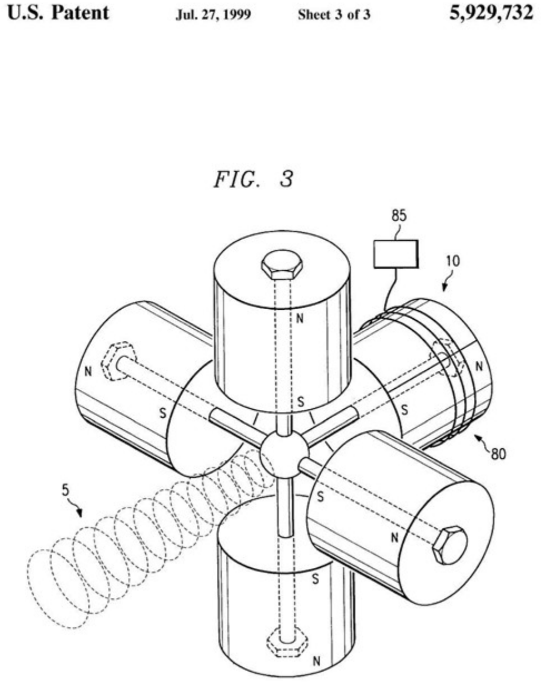

FIG. 4. The original Lockheed Martin Corporation magnetic beam amplification apparatus (U.S. Patent 5,929,732 [45]), the topological precursor to the partially-hybridized MADA cores deployed in both SHD and ADPG GU-RVG hardware. The axially-stacked ring-magnet geometry, with all poles converging on a central frustration zone, is the canonical building block for both Tier I and Tier II implementations.

A. Flux Frustration and Magnetic Helicity

The MADA geometry is a hierarchical extension of the magnetic beam amplification apparatus disclosed in U.S. Patent 5,929,732 [45], reproduced in Fig. 4. The fundamental module consists of an axially stacked arrangement of ring-magnet assemblies whose poles converge upon a central zone. The opposing poles compress the magnetic flux lines laterally and direct them collectively at highly confined 10–100 μm micro-gaps within the targeted laminated magnetic-circuit wall, where 0.15–0.35 mm laminations separated by micron-scale dielectric gaps create gradient micro-singularities and a localized region of extreme magnetic pressure (formalized as Regime 3 of the three-regime pressure budget in Sec. V A).

This flux frustration does not merely compress the energy density; it actively creates macroscopic magnetic helicity [34]:

$$H_m = \int_V \boldsymbol{A} \cdot \boldsymbol{B} \, d^3x. \tag{6}$$

H_m is a rigorous topological invariant that measures the knottedness, twisting, and linkage of magnetic field lines. In the MADA core, the absolute pole opposition imposed within the micro-gap creates a highly frustrated topological defect for which $\boldsymbol{A} \cdot \boldsymbol{B} \neq 0$. According to the holographic dictionary, the Chern-Simons terms within the bulk Observerse couple directly to this boundary magnetic helicity [3, 20].

B. Topologically Induced Phase Transitions and the Scaling Paradox

The creation of magnetic helicity resolves the profound scaling paradox inherent in metric engineering. Standard vacuum-polarization calculations indicate a critical field threshold $B_{\text{crit}} \sim 1.53 \times 10^{20}$ T at the Schwinger limit, rendering macroscopic engineering apparently impossible by brute-force thermodynamic energy density [21, 28].

The 14-dimensional bulk, however, cannot absorb the topological defect created by an opposed field. The Observerse can absorb the raw energy of an unopposed field as a thermodynamic heat sink, but it *cannot* absorb nonzero magnetic helicity [3]. This topological stress acts as a chemical potential that drives the dilaton through a spontaneous phase transition, condensing into a macroscopic holographic superconductor at the phenomenological phase boundary, which is extrapolated to lie at $B_{\text{opposing}} \approx 20\text{–}90^{+}$ T of opposed virtual pressure depending on the mass of the surrounding apparatus [3, 20].

This Topologically Induced Phase Transition shifts the system abruptly from a perturbative single-particle scaling regime into a non-perturbative, macroscopic N^2-scaling state, freezing the vacuum refractive index onto the highly helical magnetic geometry of the MADA core. The physical realization of vacuum levitation thus depends entirely upon the capacity of the magnetic material to sustain the absolute South-South (or North-North) pole opposition within the micro-gap without failure.

V. EVALUATING THE MAGNETIC MATERIAL LANDSCAPE

The engineering parameters demand a material capable of maintaining intense magnetization against its own self-demagnetizing fields and of structurally surviving the array-internal Maxwell stresses transmitted between opposing MADA modules. As established in Sec. V A below, the partially-hybridized MADA architecture imposes *three* physically distinct pressure regimes simultaneously, each acting on a different physical region and each driving a different material design choice; a single "$\sim$ 1000 MPa" figure quoted without context conflates pressures that arise from different physics. Should the magnetic material's intrinsic coercivity prove insufficient against the array-internal demagnetizing field, the opposing fields will simply re-orient the magnetic domains, destroying the flux frustration, collapsing the magnetic helicity, and instantly neutralizing the metric bubble.

The partially-hybridized MADA array imposes two physically distinct material roles, which we evaluate separately throughout this work. The *magnetic-material* role refers to the hard, permanent-magnet substrate that sources and sustains absolute South-South (or North-North) pole opposition and the intense back-pressure required to direct the combined flux through the 10–100 μm micro-gaps within the targeted laminated magnetic-circuit wall (containing 0.15–0.35 mm laminations and micron-scale dielectric gaps); this role demands extreme intrinsic coercivity, high remanence, and thermal stability. The *magnetic-circuit-material* role refers to the soft, high-permeability substrate that routes the flux through the return yokes and servo-driven flux-shunting irises without incurring large hysteresis losses; this role demands ultra-high μ_r, low coercivity, and low core loss under pulsed excitation. The two roles are physically incompatible within a single homogeneous phase: the same property (high H_c) that qualifies a candidate for permanent-magnet duty disqualifies it from soft-yoke duty, and vice versa. Tables I and II evaluate the candidate landscape against each role independently.

A. The Three-Regime Pressure Budget

The partially-hybridized MADA architecture imposes Maxwell stresses simultaneously on three physically distinct regions, and the magnetic-material design must be evaluated against all three. A single "$\sim$ 1000 MPa" figure cited without context conflates pressures that arise from different physics and that drive different material design choices, so we enumerate the regimes here for use throughout the rest of this work.

TABLE I. Comparative evaluation of candidate *magnetic-material* (permanent-magnet) substrates for partially-hybridized MADA arrays. Saturation B_s and Curie temperature T_C values are nominal; operational suitability is assessed against the hard-substrate requirements common to both SHD and ADPG MADA arrays (sustained South-South or North-North opposition, T_{op} up to ~ 500 K, recursive 300-magnet arrays). Soft alloys such as Hiperco-50 and Minnealloy are excluded by definition; they are evaluated as *magnetic-circuit-material* candidates in Table II.

Material Class	**Composition**	**Saturation B_s (T)**	**Thermal Limit T_C**	**Suitability for MADA Arrays**
Rare-Earth	$Nd_2Fe_{14}B$	~ 1.6	$\sim 310°C$	High performance; geopolitically constrained
Rare-Earth (High-T)	Sm_2Co_{17}	1.1–1.2	$\sim 820°C$	Exceptional thermal stability; highly expensive, constrained
Metastable Nitride	α''-$Fe_{16}N_2$	2.9–3.1	$< 250°C$ (decomp.)	Giant B_s; fatal thermal instability
Meteoritic	$L1_0$-FeNi (Tetrataenite)	~ 1.6	$\sim 550°C$	RE-free; not yet industrially synthesizable
Hard Ferrite	$SrFe_{12}O_{19}$	~ 0.4	$\sim 450°C$	Ultra-low cost commodity; insufficient energy density
Phosphide Alloy	$\mathbf{(Fe_{0.92}Co_{0.08})_2(P_{0.78}Si_{0.22})}$	**1.6–1.8**	$\mathbf{> 500°C}$	**Tier I—rare-earth-free;** **commodity-elemental**
$\mathbf{ThMn_{12}}$ Composite	**HeliFe-MADA hard phase**	$\mathbf{\sim 2.7}$	$\mathbf{> 1100}$ **K**	**Tier II hard pole tips;** **premium fabrication**

Regime 1 (inter-mada reciprocal pressure on array magnets). Within the five-MADA array, the four non-rear MADA modules are arranged in two opposing pairs: each pair places one MADA emitting a virtual $B_0 \approx 40.6$–108 T against another emitting the same, separated by a gap $d \gtrsim L_{\mathrm{magnet}}$ (the unopposed rear MADA experiences only the back-reaction of sourcing the array's central frustration zone and is in a much milder regime). Because the gap is comparable to the source dimension, the geometry sits in the near-field regime where the projected field at each opposing MADA face does not significantly attenuate, and the reciprocal Maxwell stress on the constituent magnet pole faces is

$$P_1 = \frac{B^2}{2\mu_0} \sim 10^2\text{–}10^3 \text{ MPa}, \tag{7}$$

with ~ 1000 MPa as a representative figure. Regime 1 sets the demagnetization-survival requirement on the magnetic substrate (Tier I core-shell pinning architecture, Tier II exchange-spring coupling) and the mechanical-containment requirement on the gimbal-mounted exoskeleton (Ti-6Al-4V / Inconel 718, with Si_3N_4/ZrO_2 ceramic spacers between adjacent MADA modules within the array).

Regime 2 (macroscopic projection onto the targeted laminated wall area). The five-MADA array projects its combined frustrated emission—a virtual $B_{\mathrm{proj}} \approx 203$–540 T linear superposition of all 300 constituent magnets—toward a gimbal-targeted point on the surrounding laminated magnetic circuit, in a manner figuratively analogous to a projecting magnetic source rather than a coherently focused beam. Geometric dispersion between the array and the targeted wall area attenuates this virtual figure substantially; assuming a representative dispersion factor of ~ 10–25%, the actual macroscopic B delivered to the targeted wall surface is $B_{\mathrm{wall,\,macro}} \approx 50$ T, which through

$$P_2 = \frac{B^2_{\mathrm{wall,\,macro}}}{2\mu_0} \approx 1000 \text{ MPa} \tag{8}$$

yields a macroscopic Maxwell stress at the targeting footprint of the surrounding wall coincidentally equal in order of magnitude to Regime 1, but arising from entirely different physics and acting on entirely different hardware. The exact dispersion factor is airframe-geometry-dependent and is treated here as a specification rather than a derivation. Regime 2 sets the structural specification for the surrounding spherical, discoidal, or cylindrical laminated magnetic circuit.

Regime 3 (microscopic concentration within the targeted lamination). The macroscopic ~ 50 T projection captured at the targeted wall area is then channeled through the high-μ laminations (where the iron-region B is bounded by $J_s \approx 2.4$–2.7 T) and forced across the 10–100 μm dielectric interlayers between the 0.15–0.35 mm laminations. At the cross-gap discontinuities, geometric flux concentration raises the local microscopic B above the macroscopic projection, with corresponding Maxwell stresses

$$P_3 \gg 1000 \text{ MPa} \tag{9}$$

over micron-scale features. This is the regime in which the propulsive $\nabla(\boldsymbol{B}\cdot\boldsymbol{B})$ singularity actually develops, and against which the *in-situ* printed Al_2O_3/ZrO_2 ceramic interlayers of the Tier II monolithic build (Sec. VII E 3) must locally contain the flux structure.

The ~ 1000 MPa figure quoted throughout this work therefore applies, coincidentally through different physics, to both Regime 1 (on the array-internal magnets) and

Regime 2 (on the targeted wall area), with Regime 3 strictly exceeding it locally over micron-scale features. Stacking multiple arrays multiplies the Regime 2 macroscopic projection proportionally; in the gimbaled multi-array airframe configuration of Sec. IX, the integrated reaction force at the targeted wall point is the macroscopic source of the propulsive integral $\boldsymbol{F}_{\mathrm{lift}}$ in Eq. (5). All subsequent invocations of the ~ 1000 MPa scale or of the 203–540 T virtual emission in this work refer back to one of these three regimes by number.

B. The Deficiencies of NdFeB and Rare-Earth Magnets

Historically, the implementation of compact recursive MADA geometries was enabled by the discovery of neodymium-iron-boron ($Nd_2Fe_{14}B$) magnets in 1984 [46]. Neodymium magnets provide the high remanence and massive intrinsic coercivity required to enforce South-South (or North-North) opposition without flux bridging. The requirement to scale this technology from laboratory proof-of-concept to mass-produced aerospace propulsion arrays, however, renders NdFeB untenable. A single compound MADA array requires hundreds of precisely machined ring magnets; scaling to fleet-level production encounters severe geopolitical and economic constraints. The global market for neodymium materials is heavily consolidated, subject to volatile pricing, and characterized by severe supply-chain vulnerabilities [6]. Furthermore, the extraction and refinement of the heavy rare-earth elements required to extend the temperature tolerance of NdFeB—particularly dysprosium and terbium—generate highly hazardous, radioactive environmental waste.

C. The Metastability of α''-$Fe_{16}N_2$

To bypass rare-earth dependency, theoretical models for permanent-magnet duty frequently invoke martensitic α''-$Fe_{16}N_2$ [50, 52, 53]. This body-centered tetragonal iron nitride exhibits a giant saturation magnetization of $\sim$2.9–3.1 T together with the uniaxial anisotropy required of a hard-magnetic substrate. The massive saturation arises from a combination of epitaxial strain and interstitial nitrogen occupying octahedral sites in the body-centered tetragonal iron lattice, which localizes the $3d$ electrons and prevents the magnetic moment from being quenched by hybridization [51]. We emphasize that α''-$Fe_{16}N_2$ is the hard, magnetic-material candidate; the chemically related but functionally distinct Minnealloy phases developed by the same research community are soft and are evaluated separately as magnetic-circuit-material candidates in Sec. V D.

While α''-$Fe_{16}N_2$ represents the theoretical ideal for achieving deep metric displacement, it possesses a fatal engineering flaw: it is thermodynamically metastable [54, 56]. At temperatures exceeding 200–250°C the interstitial nitrogen atoms rapidly diffuse out of their ordered positions, the crystalline structure decomposes into standard α-iron and the iron-nitride phase γ'-Fe_4N, and the giant magnetic moment is permanently destroyed. In the operational environment of an ADPG array (i.e., not SHD), where localized eddy currents and ambient environmental heat are significant, a thermal ceiling of 250°C provides an unacceptably narrow safety margin [56].

D. Magnetic-Circuit-Material Candidates: Hiperco-50, Minnealloy, and the Tier II Soft Yoke

The magnetic-circuit-material role—the soft, high-permeability substrate that routes flux through the return yokes and servo-driven flux-shunting irises—imposes a complementary set of requirements: ultra-high relative permeability ($\mu_r \gtrsim 10^4$–10^6), low coercivity to minimize hysteretic loss under pulsed excitation, and high T_C to remain ferromagnetic across the full operational thermal envelope. Three classes of candidate are evaluated in Table II.

Hiperco-50 (Fe-49Co-2V). Commercial iron-cobalt-vanadium alloys offer massive thermal stability ($T_C =$ 940°C) and an excellent saturation limit of 2.40 T [47–49]. Hiperco-50 possesses virtually zero intrinsic coercivity, which disqualifies it as a permanent-magnet substrate but renders it ideal for the soft-magnetic circuit elements of the ADPG, where it carries the temporal-asymmetry pulses driven by megawatt-class pulsed electromagnetic coils [7]. A Hiperco-50 core placed in South-South (or North-North) opposition would demagnetize immediately, but a Hiperco-50 *return yoke* routes flux losslessly between the permanent-magnet poles. Hiperco-50 is therefore a magnetic-circuit-material candidate, not a magnetic-material candidate.

Minnealloy (Fe-N-family soft phase; α'-Fe_8(NC)). Minnealloy, developed by the University of Minnesota magnetism group, is a separately-engineered iron-nitride soft alloy that exploits the same interstitial-nitrogen lattice expansion as α''-$Fe_{16}N_2$ to push saturation toward $\sim$ 2.9 T while retaining low coercivity [55]. Despite its chemical kinship with the hard α''-$Fe_{16}N_2$ phase discussed in Sec. V C, Minnealloy is functionally a soft magnetic alloy and is therefore a circuit-material candidate, not a permanent-magnet candidate. It inherits the same metastability constraint: above $\sim$ 250°C the interstitial nitrogen diffuses, the giant-B_s collapses, and the alloy reverts to ordinary soft α-iron behavior [54, 56]. For low-temperature, low-duty-cycle circuit applications Minnealloy offers a giant-B_s alternative to Hiperco-50; for sustained high-temperature ADPG duty cycles it is unsuitable.

Tier II soft return yoke (bcc Fe-Co exchange-spring phase). The Tier II HeliFe-MADA architecture detailed in Sec. VII is a functionally-graded exchange-spring nanocomposite whose soft return-yoke phase consists of coarsened bcc Fe-Co nanoclusters delivering

$\mu_r > 10^6$ for low-loss flux shunting (Fig. 6). Because this soft phase is monolithically printed in the same MF-L-PBF build as the hard pole tips, the Tier II material spans both roles simultaneously—a property no other candidate in either Table I or Table II possesses. Furthermore, the in-situ deposition of micro-layers of electrically insulating ceramic during the monolithic build effectively laminates the soft yokes themselves, suppressing eddy-current losses under pulsed excitation far below the level achievable with conventional stacked-sheet cores such as Hiperco-50.

The two-table evaluation makes the role coverage of each tier explicit. Tier I addresses only the magnetic-material role (Table I); a Tier I airframe still requires a separate soft-yoke substrate—typically Hiperco-50—to complete the MADA flux circuit. Tier II addresses both roles within a single monolithic build; the same MF-L-PBF process that produces the hard Tier II pole tip also produces the soft Tier II return yoke, eliminating the joint between dissimilar materials and the associated reluctance penalty.

VI. TIER I: THE IRON-PHOSPHIDE GAP MAGNET $(\mathrm{Fe}_{0.92}\mathrm{Co}_{0.08})_2(\mathrm{P}_{0.78}\mathrm{Si}_{0.22})$

To populate MADA arrays at the volume and cost demanded by global civilian and commercial deployment, the magnetic material must combine the coercivity of a rare-earth magnet, the thermal stability of a commercial iron-cobalt alloy, and the economic scalability of commodity rock-forming elements. The Tier I solution to this multi-variable optimization problem is the highly engineered iron-phosphide alloy $(\mathrm{Fe}_{0.92}\mathrm{Co}_{0.08})_2(\mathrm{P}_{0.78}\mathrm{Si}_{0.22})$ [57, 58]. Tier I is fully compatible with both SHD and ADPG hardware—each of which uses partially-hybridized MADA arrays—and is the recommended material for any deployment in which the unit-cost-per-magnet must be bounded by commodity supply chains.

Developed through extensive ab-initio density-functional-theory calculations and subsequent single-crystal synthesis [58, 60], this specific stoichiometry constitutes a breakthrough in gap-magnet technology. The base material, binary iron phosphide ($\mathrm{Fe}_2\mathrm{P}$), crystallizes in the hexagonal $P\bar{6}2m$ space group, supplying the foundational uniaxial crystal structure required for an anisotropic crystal field. In its pure form, binary $\mathrm{Fe}_2\mathrm{P}$ exhibits substantial magnetocrystalline anisotropy but suffers from a low Curie temperature of 216 K, rendering it paramagnetic at room temperature [62].

A. Substitutional Crystallography and Property Tuning

The engineering of the quaternary alloy $(\mathrm{Fe}_{0.92}\mathrm{Co}_{0.08})_2(\mathrm{P}_{0.78}\mathrm{Si}_{0.22})$ rests on highly specific atomic site substitutions that independently tune the critical magnetic parameters required by the MADA arrays.

Cobalt for iron ($3f$, $3g$ sites). Cobalt selectively substitutes for iron at the $3f$ and $3g$ crystallographic sites. Orbital hybridization between the transition-metal states strongly enhances the ferromagnetic exchange interactions. This cobalt substitution lifts the Curie temperature T_C of the alloy well above 500 K, providing exceptional thermal stability that vastly exceeds the operational requirements of any partially-hybridized MADA array—whether deployed in SHD, ADPG, or SHD-with-embedded-ADPG configurations—and completely bypasses the metastability issues that plague α''-$\mathrm{Fe}_{16}\mathrm{N}_2$ [57, 59].

Silicon for phosphorus ($2c$ sites). Silicon selectively substitutes for phosphorus at the $2c$ non-metal sites. Silicon doping serves two critical functions. Most importantly, it maximizes the uniaxial magnetocrystalline anisotropy constant K_1. Empirical measurements on single crystals of this exact stoichiometry confirm $K_1 \approx 1.09$ MJ/m^3 at room temperature [58]. This immense intrinsic anisotropy is the foundational prerequisite for high coercivity. In addition, silicon doping suppresses the problematic first-order magnetoelastic phase transition characteristic of binary $\mathrm{Fe}_2\mathrm{P}$, converting it to a stable second-order transition and eliminating short-range magnetic order above T_C [58, 61]. The material is thereby protected against spontaneous structural volume changes and abrupt losses of magnetization under the varying thermal loads of the MADA environment.

The precise $(\mathrm{Fe}_{0.92}\mathrm{Co}_{0.08})_2(\mathrm{P}_{0.78}\mathrm{Si}_{0.22})$ stoichiometry optimizes the delicate balance between these substitutions, yielding a substantial saturation specific magnetization and a theoretical maximum energy product

$$(BH)_{\max} \approx 180\ \mathrm{kJ/m^3} \approx 22.6\ \mathrm{MGOe}. \tag{10}$$

This places the material firmly in the gap-magnet category, vastly outperforming hard ferrites and alnico magnets by factors of three to five while requiring zero strategic rare-earth elements [57].

B. Microstructural Engineering for Extreme Coercivity

Although the intrinsic properties of $(\mathrm{Fe}_{0.92}\mathrm{Co}_{0.08})_2(\mathrm{P}_{0.78}\mathrm{Si}_{0.22})$—its high saturation magnetization M_s and immense magnetocrystalline anisotropy K_1—are established in the single-crystal form, single crystals do not inherently exhibit the massive coercivity required to survive the South-South (or North-North) flux-frustration zone. In bulk crystalline form, magnetization reversal proceeds easily through the unhindered nucleation and propagation of magnetic domain walls. Transitioning the material from a high-anisotropy crystal into a high-coercivity permanent magnet capable of metric engineering therefore demands precise microstructural control [64, 65].

TABLE II. Comparative evaluation of candidate *magnetic-circuit-material* (soft-yoke and flux-shunting iris) substrates for partially-hybridized MADA arrays. These materials are excluded from Table I because their near-zero coercivity demagnetizes immediately under South-South (or North-North) opposition; they are required for the complementary soft-yoke role, in which flux is routed losslessly between the permanent-magnet poles.

Material Class	**Composition**	**Saturation B_s (T)**	**Thermal Limit T_C**	**Suitability for Yoke / Iris Role**
Soft Fe-Co Alloy	Fe-49Co-2V (Hiperco-50)	2.40	940°C	Mature, high-T_C; canonical ADPG yoke
Electrical Steel	Fe-3%Si	~ 2.0	740°C	Industry standard, cheap; moderate saturation limit
Nanocrystalline	FINEMET (Fe-Si-B-Nb-Cu)	1.2–1.3	~ 570°C	Ultra-low core loss; limited saturation limit
Soft Fe-N Alloy	Minnealloy (α'-Fe_8(NC))	~ 2.9	< 250°C (decomp.)	Giant B_s; low-temperature use only
Tier II Soft Yoke	**bcc Fe-Co (FGM region)**	**~ 2.4**	**> 1100 K**	**$\mu_r > 10^6$; monolithic with hard pole tips (no joint)**

1. *Sub-Micron Grain Refinement*

The primary mechanism for coercivity development in the iron-phosphide alloy is the reduction of the physical grain size below the critical single-domain threshold. When particles are reduced to the sub-micron scale—calculated to be approximately 773 nm for similar highly anisotropic alloys [64]—the formation of multi-domain structures within a single grain becomes energetically unfavorable. Each grain therefore acts as a single, massive magnetic dipole. Magnetization reversal can no longer proceed via the low-energy mechanism of domain-wall motion; it must occur through coherent rotation of the entire magnetization vector against the strong uniaxial anisotropy field of the hexagonal lattice [65].

This requirement dictates the fabrication methodology. The material cannot be cast or forged. Instead, the precursor alloy is subjected to high-energy planetary ball milling in an inert argon atmosphere to fracture the crystalline structure down to a homogeneous, sub-micron powder. The duration of the milling process—typically up to 24 h—is strictly controlled to ensure a narrow particle-size distribution that maximizes the volume fraction of single-domain grains.

2. *Grain-Boundary Pinning and Trace-Element Doping*

While single-domain particle sizing supplies the baseline coercivity, the Regime 1 reciprocal demagnetizing fields developed between opposing MADA modules within the array (Sec. V A) necessitate secondary reinforcement to prevent cascading demagnetization. The 203–540 T figure cited elsewhere is the linear-superposition virtual emission of the array projected toward the targeted laminated wall (Regime 2), not the field experienced by the magnets internally; the relevant array-internal driver here is the near-field reciprocal Maxwell stress on the magnet pole faces, of order 10^2–10^3 MPa per Eq. (7). If the single-domain grains are in direct physical and magnetic contact, exchange coupling across the grain boundaries can permit magnetization reversal to nucleate at a surface defect and sweep rapidly through the entire bulk material [65].

To isolate the grains and pin any nucleating domain walls, the base $(Fe_{0.92}Co_{0.08})_2(P_{0.78}Si_{0.22})$ stoichiometry is modified with trace additions of 0.5–2.0 at.% of non-magnetic or antiferromagnetic pinning elements, specifically aluminum or manganese. During the subsequent sintering phase these trace elements preferentially segregate to the grain boundaries, forming a thin, non-magnetic or weakly magnetic intergranular shell around the highly magnetic iron-phosphide cores. This core-shell architecture (Fig. 5) provides absolute magnetic isolation between adjacent sub-micron grains. The intergranular phase acts as a physical barrier that pins domain walls and ensures that the demagnetization of one misaligned grain does not trigger reversal of its neighbors. The inclusion of manganese is particularly synergistic: manganese atoms occupying the $3g$ crystallographic sites enhance local magnetic moments while simultaneously disrupting inter-grain exchange coupling [63]. This grain-boundary engineering drives the intrinsic coercivity H_{cj} into the 5–12 kOe range, providing the magnetic rigidity required to maintain the South-South (or North-North) opposition topology without flux bridging.

C. Scalable Fabrication for MADA Architectures

The architectural requirement of any GU-RVG hardware—whether SHD, ADPG, or a hybrid SHD airframe with an embedded ADPG burst-mode module—mandates the production of complex, recursive fractal geometries. A single full-scale implementation requires multiple partially-hybridized MADA arrays, each consisting of 60-magnet modules arrayed in 12-ring stacked assemblies, totaling hundreds of individually precision-oriented magnetic components [6, 7]. The economic and logistical viability of this propulsion-and-power paradigm depends entirely on

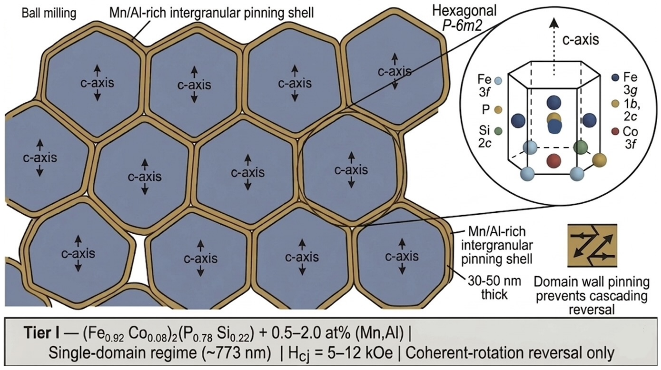

FIG. 5. Tier I sub-micron core-shell microstructure of $(\mathrm{Fe}_{0.92}\mathrm{Co}_{0.08})_2(\mathrm{P}_{0.78}\mathrm{Si}_{0.22})$ following high-energy ball milling and Spark Plasma Sintering. The hexagonal $P\bar{6}2m$ $\mathrm{Fe_2P}$-type cores (sub-micron, single-domain, with the *c*-axis aligned by the green-state magnetic field) are separated by a thin non-magnetic Mn/Al-rich intergranular shell that pins domain walls and prevents cascading reversal under the 10^2–10^3 MPa Regime 1 inter-MADA reciprocal demagnetization pressures (Sec. V A, Eq. 7) developed within the array between opposing MADA modules. Coherent rotation against the uniaxial anisotropy field is the only available reversal pathway, yielding intrinsic coercivity $H_{cj} = 5$–12 kOe.

TABLE III. Fabrication sequence for $(\mathrm{Fe}_{0.92}\mathrm{Co}_{0.08})_2(\mathrm{P}_{0.78}\mathrm{Si}_{0.22})$ MADA ring magnets and the metric-engineering benefit conferred at each stage.

Stage	Process	Benefit
Powder prep.	Planetary ball mill, 24 h, Ar atm.	Sub-micron single-domain grains
Green compaction	Iso/uniaxial press, 0.5–1.0 T align field	*c*-axis alignment, max. B_r
Consolidation	SPS or microwave sinter, 1000–1100°C, 30 s–10 min	> 95% density; arrests grain growth
Post-process	Low-T anneal	Mn/Al pinning at grain boundaries

the manufacturing profile of the core material.

The $(\mathrm{Fe}_{0.92}\mathrm{Co}_{0.08})_2(\mathrm{P}_{0.78}\mathrm{Si}_{0.22})$ alloy excels in this domain because its elemental constituents—iron, phosphorus, and silicon—are among the most abundant and inexpensive rock-forming elements on Earth. Cobalt is required only as a minor dopant (8 at.% of the transition-metal sites), minimizing exposure to its localized supply chains. Furthermore, the required fabrication route leverages established, scalable powder-metallurgy techniques identical to those used in the mature hard-ferrite industry, completely avoiding the vacuum induction melting and hydrogen decrepitation required for NdFeB [46].

During the compaction phase, a strong external aligning field (≈ 0.5–1.0 T) is applied uniaxially or circumferentially. Because the sub-micron grains are single-domain and free to rotate within the uncompacted powder, the aligning field forces the *c*-axis (the easy axis of magnetization for the hexagonal $P\bar{6}2m$ lattice) of every particle into perfect alignment with the target vector. This magnetic texturing produces maximum anisotropic remanence B_r in the required pole direction, preventing flux leakage and maximizing the spatial gradients $\nabla(\boldsymbol{B}\cdot\boldsymbol{B})$ demanded by Eq. (5).

The aligned green compacts are subjected to rapid reactive sintering. Conventional prolonged sintering risks excessive grain growth, which would push the particles out of the single-domain regime and destroy the coercivity. The process therefore employs short-cycle Spark Plasma Sintering (SPS) or microwave sintering [66, 67]: high pulsed direct current is applied through the die under vacuum at 1000–1100°C for between 30 s and 10 min, achieving greater than 95% theoretical density while strictly arresting grain-boundary migration. The rapid consolidation preserves both the sub-micron grain structure and the non-magnetic trace-element pinning layers. The resulting net-shape rings require minimal post-machining, completely avoiding the catastrophic material waste associated with the slicing and grinding of sintered NdFeB blocks.

VII. TIER II: THE HELIFE-MADA ARCHITECTURE FOR HIGH-PERFORMANCE OPERATION

While the Tier I iron-phosphide alloy provides an economically scalable solution suitable for civilian mass deployment, the absolute upper limit of the Master Equation of Levitation is bounded by the saturation polarization J_s achievable by the material. The Slater-Pauling rule fixes a hard ceiling at $J_s \approx 2.45$ T near the binary $\mathrm{Fe}_{65}\mathrm{Co}_{35}$ composition [68, 69]. To unlock the high-performance regime—particularly for exquisite military and intelligence platforms and for high-end consumer applications where saturation, intrinsic chirality, and pulsed-burst tolerance must be maximized irrespective of unit cost—we propose the HELIFE-MADA architecture: a chirally-doped, interstitially-stabilized ThMn_{12}-type exchange-spring nanocomposite engineered to simultaneously transcend the Slater-Pauling barrier and source macroscopic magnetic helicity from the bulk alloy itself. Tier II is fully compatible with both SHD and ADPG hardware; in particular, when integrated into a SHD airframe alongside an embedded ADPG module for burst-mode vacuum liquefaction (Sec. IX), the intrinsic chirality of the Tier II core relieves the MADA flux-frustration topology of the burden of sourcing helicity entirely on its own.

A. Transcending the Slater-Pauling Barrier via the Magnetovolume Effect

In conventional condensed-matter physics, the Slater-Pauling curve sets the maximum magnetic moment achievable in transition-metal alloys [68]. The peak occurs at $\mathrm{Fe}_{65}\mathrm{Co}_{35}$, yielding approximately 2.45 T or $\sim 2.4\,\mu_B$ per

TABLE IV. Comparison of magnetic-moment ceilings across material classes. The HeliFe-mada Tier II target ($J_s \approx 2.7$ T) sacrifices a controlled fraction of the metastable-nitride moment in exchange for thermodynamic robustness suitable for repetitive pulsed ADPG operation.

Class	Composition	m (μ_B/at.)	J_s (T)
Pure Iron	α-Fe	2.22	2.15
Slater-Pauling peak	$Fe_{65}Co_{35}$	2.40	2.45
Metastable nitride	α''-$Fe_{16}N_2$	2.9–3.0	2.9–3.1
Tier II	**Fe-Co-V-N (doped)**	**~ 2.7**	**2.7**

atom. This limitation arises from the progressive filling of majority and minority d-band states: once the majority states are saturated, additional valence electrons populate the minority states, reducing the net spin imbalance and quenching the magnetic moment.

To break this barrier and reach $J_s \approx 2.7$ T, the HeliFe-mada architecture leverages *interstitial modification* rather than further substitutional alloying. The introduction of interstitial nitrogen (or carbon, or boron) into a body-centered tetragonal (bct) or $ThMn_{12}$-type lattice triggers a profound *magnetovolume effect* [50, 52, 70, 71]. Interstitial nitrogen atoms occupy specific octahedral sites, inducing highly directional epitaxial strain that physically expands the host lattice. The resulting volumetric expansion increases the interatomic Fe–Co distance and narrows the $3d$ electron bands. The reduced bandwidth diminishes the spatial overlap of the electron wavefunctions and causes the $3d$ electrons to localize. Extreme localization suppresses s–d hybridization and significantly enhances the exchange splitting between spin-up and spin-down bands.

The resulting "giant" magnetic moment—first identified in metastable phases such as α''-$Fe_{16}N_2$ and the complex Minnealloy derivative α'-$Fe_8(NC)$—can reach saturation magnetizations of 2.8–3.1 T, far exceeding the Slater-Pauling limit [50, 53, 55, 72]. The HeliFe-mada alloy adopts this interstitial nitrogenation strategy but *stabilizes* a target $J_s \approx 2.7$ T. The deliberate sacrifice of a fraction of the metastable-nitride moment provides a robust engineering margin for the $B_{\text{opposing}} \approx 20$–$90^{+}$ T (mass dependent) opposed-gap fields while remaining thermodynamically stable enough for sustained high-frequency pulsed operation, comfortably exceeding the 1.6–1.8 T ceiling of the Tier I alloy.

B. Topological Helicity and Dzyaloshinskii-Moriya Engineering

Raw energy density alone is insufficient: the Tier II material must be *chirally active* to fulfill the boundary condition $H_m \neq 0$ intrinsically rather than relying solely on macroscopic flux frustration. To this end, the HeliFe-mada alloy must host *antisymmetric exchange interactions*—the Dzyaloshinskii-Moriya interaction (DMI)—which becomes active when spatial inversion symmetry is broken in the presence of strong spin-orbit coupling (SOC) [82–84]. The DMI Hamiltonian takes the cross-product form

$$H_{\text{DMI}} = \sum_{i \neq j} \boldsymbol{D}_{ij} \cdot (\boldsymbol{S}_i \times \boldsymbol{S}_j), \tag{11}$$

in which the chirality of the interaction between spins $\boldsymbol{S}_i$ and $\boldsymbol{S}_j$ is set by the direction and magnitude of the Dzyaloshinskii-Moriya vectors $\boldsymbol{D}_{ij}$.

1. Heavy-Metal Chiral Dopants: Pt, Ir, Mn

To engineer DMI within the bulk HeliFe-mada matrix, specific chiral dopants—heavy transition metals such as platinum (Pt) and iridium (Ir)—are substituted at low atomic percentages (0.1–1 at.%) [85, 86]. These heavy elements possess massive spin-orbit coupling. When asymmetrically substituted into the Fe-Co sublattices, they create localized nanoscale regions entirely lacking spatial inversion symmetry. The Fert-Levy mechanism then drives DMI through conduction-electron scattering, favoring twisted, orthogonal alignment of neighboring spins over collinear ferromagnetic alignment.

Manganese (Mn) doping is used concurrently to tune the DMI strength and to dictate the rotational sign of the helicity [84, 88]. In Fe-Co systems the precise substitution of Mn alters the $3d$ electron-band filling, which directly controls the chirality (left-handed versus right-handed) of the resulting spin textures. By balancing Pt or Ir for SOC against Mn for band-filling control, the HeliFe-mada alloy natively stabilizes helical spin structures and skyrmion lattices at room temperature and beyond [89]. This intrinsic, bulk chirality guarantees that, as the material is magnetized within the MADA array, the heavily compressed flux lines do not remain planar; instead, they twist into stable helical configurations and instantaneously generate the macroscopic helicity density required to seed the boundary Chern-Simons coupling and trigger dilaton condensation [34, 90, 91].

C. Compositional Architecture and Phase Stabilization

To satisfy the inherently contradictory requirements of ultra-high saturation, extreme coercivity, structural stability, and spontaneous chiral topology, the HeliFe-mada alloy diverges entirely from simple binary Fe-Co matrices and from rare-earth-heavy Nd-Fe-B systems. The proposed baseline stoichiometry is a multi-component, interstitially-stabilized, chirally-doped $ThMn_{12}$-type structure:

$$Nd_{0.05}(Fe_{0.68}Co_{0.17}V_{0.05})_{11.5}N_{0.05} + \text{tr. (Pt, Ir, Mn)}. \tag{12}$$

TABLE V. Compositional architecture of the HeliFe-mada alloy and the functional role of each constituent in the GU-RVG metric-engineering chain.

Element	at.%	Functional role
Fe	68	Primary magnetic-moment carrier; bulk magnetization
Co	17	Elevates $T_c > 1100$ K; boosts exchange interaction
Nd	5	Provides basal uniaxial K_1 for coercivity
V	5	Thermodynamic stabilizer for $\mathrm{ThMn_{12}}$ lattice
N	5	Interstitial expansion; giant-J_s boost; K_1 multiplier
Pt/Ir/Mn	trace	Breaks inversion symmetry; induces DMI for helicity

1. *The ThMn$_{12}$-Type Backbone*

The tetragonal $\mathrm{ThMn_{12}}$-type phase ($\mathrm{REFe_{12}}$, where RE is a rare-earth element) is selected over the ubiquitous $\mathrm{Nd_2Fe_{14}B}$ (2:14:1) phase for two reasons: vastly superior intrinsic magnetic properties at elevated temperatures, and a dramatically lower rare-earth volume fraction ($\sim$ 7.7 at.% versus $\sim$ 11.8 at.%) [77–79]. The reduction in rare-earth dependency is critical for the scalable mass-production of distributed MADA arrays. However, pure binary $\mathrm{REFe_{12}}$ is thermodynamically unstable and cannot be synthesized as a bulk material. To stabilize this highly desirable phase, a precise combination of transition-metal substitution and interstitial modification is mandatory [75, 80].

Cobalt substitution. Co serves a vital dual purpose: it raises the Curie temperature T_c well beyond 1100 K, mitigating thermal demagnetization within the high-stress MADA gap, and simultaneously enhances the interatomic exchange interaction, pushing J_s toward the engineered 2.7 T target.

Vanadium and titanium stabilization. V or Ti acts as the primary thermodynamic stabilizer: these elements preferentially occupy specific lattice sites (e.g., the $8i$ sites in the $\mathrm{ThMn_{12}}$ structure) and lower the formation energy of the 1:12 structure relative to competing 2:17 phases [80].

Interstitial nitrogenation. To counteract the minor reduction in J_s caused by V/Ti substitution, interstitial nitrogen is introduced. As detailed above, nitrogenation expands the unit cell. Crucially, in the $\mathrm{ThMn_{12}}$ structure nitrogen also dramatically increases the uniaxial magnetocrystalline anisotropy constant K_1, establishing the foundational coercivity necessary to withstand the 10^2–10^3 MPa Regime 1 reciprocal demagnetization pressures developed between opposing MADA modules within the array (Sec. V A, Eq. 7) [78, 79].

D. Exchange-Spring Nanocomposite Architecture

The MADA core demands a multifunctionality that no single homogeneous magnetic phase can provide. The pole tips facing the micro-gap must exhibit massive coercivity ($H_c \gtrsim 3$ T) to resist demagnetization, while the bulk return yokes and flux-shunting irises require ultra-high relative permeability ($\mu_r > 10^6$) to amplify and route magnetic flux without incurring large hysteresis losses. To reconcile this opposition of properties within a monolithic structure, HeliFe-mada employs *exchange-spring* nanocomposite engineering [92–94].

An exchange-spring magnet combines a hard phase (providing immense coercivity) with a soft phase (providing ultra-high J_s), coupled at the nanoscale through quantum exchange interactions. For the mechanism to function, the soft grains must be smaller than twice the domain-wall width—the exchange length $l_{\mathrm{ex}} = \sqrt{A/K_1}$—of the surrounding hard phase, typically 5–20 nm [64, 65]. Under these morphological constraints, the exchange coupling forces the soft-grain magnetic moments into rigid alignment with the hard grains, preventing spontaneous reversal under reverse applied fields.

In the HeliFe-mada architecture, the hard phase consists of highly nitrogenated, Nd-substituted $\mathrm{ThMn_{12}}$ crystals that serve as massive domain-wall pinning sites; the soft phase consists of nearly pure body-centered-cubic (bcc) Fe-Co nanoclusters that provide the giant-J_s backbone [78, 94]. This core-shell topology yields a single-phase-like macroscopic behavior with theoretical energy product approaching

$$(BH)_{\max}^{\mathrm{HeliFe-mada}} \approx 1450\ \mathrm{kJ/m^3} \approx 182\ \mathrm{MGOe}, \qquad (13)$$

far surpassing both the Tier I value [Eq. (10)] and current commercial NdFeB limits. The functionally-graded zonation produced by MF-L-PBF—hard pole tips, soft return yokes, and the exchange-spring core-shell coupling that ties them together monolithically—is illustrated in Fig. 6.

The nanostructuring confers a second, vital benefit for any system that employs pulsed actuation. The ADPG, originally developed for stationary energy production, is also integrated into SHD airframes as a burst-mode vacuum-liquefaction module: it relies on temporal asymmetry—megawatt-class nanosecond pulses (dI/dt) driven by a Solid-State Marx Generator—to physically shock the local vacuum metric out of equilibrium during high-speed vector changes, preventing vacuum friction from tearing the metric bubble apart [6, 7]. Were the core a solid, conductive block, these high-frequency pulses would generate massive internal eddy-current loops; by Lenz's law, the resulting opposing fields would shield the interior of the core from the drive flux and instantly destroy the $\nabla(\boldsymbol{B}\cdot\boldsymbol{B})$ gradient demanded by Eq. (5). The exchange-spring nanostructure, separated by highly resistive grain boundaries, breaks the macroscopic conductivity paths and permits nanosecond flux penetration deep into the partially-hybridized MADA geometry of either

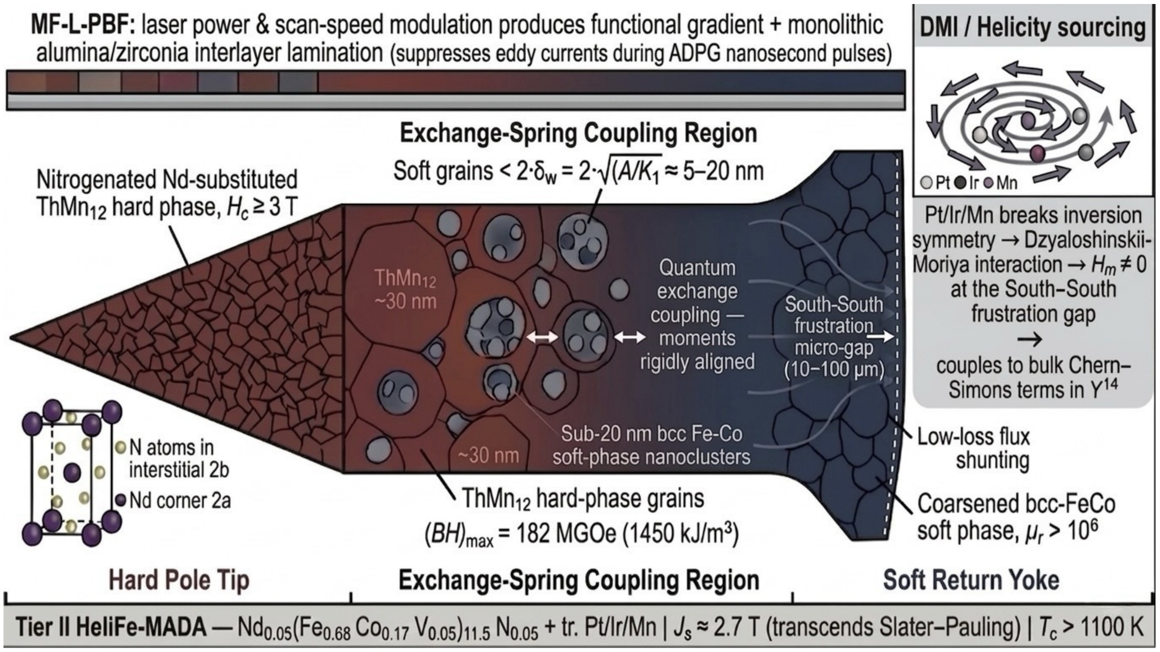

FIG. 6. Tier II HeliFe-mada functionally-graded exchange-spring architecture, monolithically printed by magnetic field-assisted laser powder-bed fusion (MF-L-PBF). *Hard zones* (pole tips, red): nitrogenated, Nd-substituted $ThMn_{12}$ crystals serve as massive domain-wall pinning sites supplying $H_c \gtrsim 3$ T. *Soft zones* (return yokes, blue): coarsened bcc Fe-Co nanoclusters supply $\mu_r > 10^6$ for low-loss flux shunting. *Exchange-spring coupling region* (interface): sub-20 nm soft grains embedded in the hard matrix and coupled via quantum exchange interactions over the exchange length $l_{\text{ex}} = \sqrt{A/K_1}$ deliver a single-phase-like macroscopic response with $(BH)_{\max}^{\text{HeliFe-mada}} \approx 182$ MGOe. *Inset:* Pt/Ir/Mn chiral dopants break inversion symmetry, activating the Dzyaloshinskii-Moriya interaction that twists the compressed flux lines into helical, skyrmionic textures with $H_m \neq 0$ at the South-South (or North-North) frustration gap.

subsystem. To complement this nanoscale resistance, the macroscopic soft return yokes are intrinsically laminated through the periodic deposition of ceramic interlayers during the MF-L-PBF process, which comprehensively suppresses large-scale eddy-current loops and protects the flux gradient.

E. Magnetic Field-Assisted Additive Manufacturing

The synthesis of highly nitrogenated, nanostructured, chiral alloys presents severe metallurgical and thermodynamic challenges. Although the interstitial-nitrogen $ThMn_{12}$ host lattice of HeliFe-mada is markedly more thermally robust than the related martensitic phase α''-$Fe_{16}N_2$—the latter evolves nitrogen catastrophically above $\sim 250°$C, whereas the heavily Co-substituted, V-stabilized $ThMn_{12}$-N host of HeliFe-mada retains its interstitial nitrogen to roughly 600–700°C, well below its magnetic Curie ceiling at $T_c > 1100$ K—conventional bulk-metallurgical routes cannot supply this material at all. Casting and forging require sustained exposure to melt temperatures that evolve *any* interstitial nitrogen pre-alloyed into the powder, and prolonged sintering would coarsen the sub-20 nm soft Fe-Co grains far past the exchange length $l_{\text{ex}} = \sqrt{A/K_1}$, dissolving the exchange-spring coupling regardless of whether the nitrogen survives [54, 73]. To bypass these limitations, HeliFe-mada relies on *magnetic field-assisted laser powder-bed fusion* (MF-L-PBF) coupled with post-consolidation *in-situ* plasma nitrogenation and localized laser modulation [96–99]. The laser-melting timescale is short enough to lock in the functionally-graded zonation; the nitrogen is then introduced *after* the nanostructure has been fixed, at temperatures well below both the nitrogen-evolution threshold and T_c.

1. *Precursor Synthesis: Vacuum Gas Atomization*

Precursor powders are generated through vacuum induction melting followed immediately by inert-gas atomization, which produces highly spherical, micrometer-scale particles of the base Nd-Fe-Co-V alloy. The extreme cooling rates inherent to gas atomization ($> 10^4$ K/s) suppress the formation of stable, low-magnetization equilibrium phases, locking the precursor material into a highly disordered nanocrystalline or amorphous state primed for laser processing [100].

2. MF-L-PBF and Functionally Graded Zonation

Consolidation of the amorphous powder into the recursive geometries of the MADA core (e.g., 60-magnet stacked-ring assemblies) is achieved through laser powder-bed fusion (L-PBF). Conventional L-PBF of brittle magnetic intermetallics typically suffers from severe microcracking, residual thermal stress, and porosity caused by keyhole instability [105]. To mitigate these defects, an external pulsed magnetic field is applied directly to the powder bed during printing [101–104]. The applied field interacts with the melt-pool hydrodynamics, generating Lorentz forces that dampen the chaotic Marangoni convection, stabilize the keyhole, and virtually eliminate porosity. Simultaneously, the magnetic field exerts a torque on the solidifying grains, physically aligning their easy-magnetization axes parallel to the applied field. This *in-situ* alignment yields a textured, macroscopically anisotropic microstructure without the need for post-process hot deformation, perfectly tailoring the flux path to follow the curved geometry of the MADA yokes and irises.

By dynamically varying the laser power, scan speed, and localized powder deposition during the build, the system modulates the thermal history of specific volumetric regions to produce a true functionally graded material (FGM) [97, 106]:

- **Soft zones (yokes and irises):** High laser power and slower scan speeds promote larger grain growth, reducing the density of domain-wall pinning sites and maximizing $\mu_r > 10^6$ for highly efficient flux shunting.
- **Hard zones (pole tips):** Lower energy density and rapid cooling preserve the sub-20 nm grain size required for exchange-spring hardening; subsequent localized laser annealing induces the order–disorder transitions needed to maximize K_1 at the pole tips, which collectively target the 10–100 μm micro-gaps within the laminated magnetic-circuit wall and ensure structural integrity against the array-internal Regime 1 reciprocal demagnetizing forces (Sec. V A, Eq. 7) of order 10^2–10^3 MPa transmitted from the opposing MADA module.

3. Monolithic Lamination via Ceramic Interlayer Deposition

The L-PBF process is further programmed to print highly resistive dielectric boundaries directly into the core. Rather than physically assembling sheets of metal, the L-PBF print head periodically deposits micro-layers of electrically insulating ceramic (e.g., alumina or zirconia) between layers of the HELIFE-MADA alloy during the build. This produces an intrinsic, monolithic laminated structure of optimal sub-millimeter thickness (≈ 0.15 mm), fully suppressing macroscopic eddy-current loops while maintaining geometric fidelity in the complex three-dimensional shape of the MADA array.

F. Post-Process Plasma Nitrogenation and Surface Passivation

Because the high-temperature laser melting process would instantly vaporize any pre-alloyed nitrogen within the powder, the critical nitrogenation step must occur *after* consolidation. To achieve optimal stabilization of the $ThMn_{12}$ and Fe-Co nanocluster phases without thermal decomposition, the fully printed MADA cores are subjected to low-temperature ($< 350°C$) inductively-coupled-plasma (ICP) nitrogenation [71, 108, 109]. The plasma field dissociates N_2 or NH_3 gas into highly reactive monoatomic nitrogen, which rapidly diffuses into the interstitial sites of the engineered nanostructure. Precise electronic control of the nitrogen fugacity within the plasma chamber ensures the optimal volumetric expansion of the lattice and achieves the giant magnetic moment without crossing the thermodynamic threshold into detrimental compound formation. A localized cobalt-rich surface passivation layer is subsequently applied at the micro-gaps to ensure long-term corrosion resistance and stability under high-frequency operation.

G. Troubleshooting, Fault Mitigation, and the HEA Fallback

1. Thermal Degradation under Active Pumping

ADPG operation generates immense resistive I^2R heating and high-frequency core losses. Although the $ThMn_{12}$-N host of the HELIFE-MADA core is far more thermally robust than the rejected α''-$Fe_{16}N_2$ candidate, the operational ceiling involves several physically distinct temperatures that should not be conflated. The magnetic Curie ceiling of HELIFE-MADA ($T_c > 1100$ K, $\sim$827°C) is set by spin-disordering thermodynamics and bounds the temperature above which M_s collapses to zero. The chemical nitrogen-evolution ceiling, set instead by interstitial diffusion kinetics in the rigid $ThMn_{12}$ host, lies at $\sim$600–700°C for the heavily Co-substituted HELIFE-MADA variant—well above the $\sim$ 250°C metastability ceiling that disqualifies α''-$Fe_{16}N_2$ and Minnealloy, and the threshold above which catastrophic, irreversible demagnetization occurs through nitrogen escape from the lattice [54, 73]. The microstructural ceiling, set by coarsening of the sub-20 nm Fe-Co soft-magnetic grains past the exchange length l_{ex}, lies lower still at $\sim$450–500°C; at this temperature the nitrogen is still chemically stable but the exchange-spring coupling that ties the soft yokes to the hard pole tips begins to dissolve. None of these is the binding constraint in practice. The actual operational ceiling for sustained pulsed-burst service is the working envelope of the dielectric coolant itself: a high-boiling perfluoropolyether (PFPE) such as Solvay Galden HT-200 ($\sim$ 270°C) or HT-270 ($\sim$ 310°C) [7], in which the core is fully immersed. The fluid permeates the micro-interstices of the laminated assembly; localized hot spots induce nucleate boiling, which absorbs massive latent heat and isothermally clamps the core well below the microstructural ceiling and dramatically below both the nitrogen-evolution and Curie ceilings of the magnetic material itself.

2. *The High-Entropy Alloy Fallback*

If interstitial-nitrogen instability proves entirely intractable for extreme high-duty-cycle pulsed service—whether in stationary ADPG energy-production installations or in ADPG modules embedded within SHD craft for burst-mode vacuum liquefaction—the HeliFe-MADA architecture can pivot from interstitial stabilization to *high-entropy alloy* (HEA) stabilization. Recent metallurgical developments in Fe-Co-Ni-Si-based HEAs demonstrate that multi-principal-element matrices can achieve yield strengths exceeding 1.1 GPa and respectable saturation magnetizations up to 1.72 T while pushing T_c to an exceptional 1169 K [107]. The massive configurational entropy of the HEA fundamentally lowers the free energy of the solid solution, providing absolute thermodynamic stability where ordered intermetallics would normally fail. Although J_s falls short of the nitrogenated HeliFe-MADA ideal, the robust mechanical and thermal integrity prevents fracture or demagnetization under the brutal magnetic pressures of the micro-gap, providing a reliable Tier II alternative for both stationary and mobile pulsed applications.

3. *Mechanical Burst Forces*

The Regime 1 reciprocal Maxwell stress between opposing MADA modules within the array (Sec. V A, Eq. 7) is profound. At an effective field of ~ 50 T at the opposing pole faces, $P_m = B^2/(2\mu_0) \approx 1000$ MPa ($\sim 10^4$ atm). Left unconstrained, the opposing MADA modules would violently fly apart from one another and destroy the assembly. Each printed MADA core must therefore be encased within a non-magnetic, high-yield-strength exoskeleton: titanium alloys (Ti-6Al-4V) or precipitation-hardened nickel-chromium superalloys (Inconel 718). To maintain accurate gimbaled targeting of the precise 10–100 μm micro-gaps within the surrounding laminated magnetic-circuit wall, specialized ceramic spacers fabricated from silicon nitride (Si_3N_4) or zirconia (ZrO_2) are inserted between adjacent MADA modules within the array. These advanced ceramics are non-magnetic, electrically insulating, and possess compressive yield strengths well in excess of 1000 MPa, sufficient to contain the Regime 1 array-internal stresses while transmitting the integrated reaction force through the gimbal mounts to the airframe.

Two further pressure budgets must be addressed by hardware outside the magnetic substrate itself. The Regime 2 macroscopic projection delivers ~ 1000 MPa Maxwell stress over the targeting footprint of the surrounding wall (Eq. 8); this is contained by the structural specification of the surrounding spherical, discoidal, or cylindrical laminated magnetic circuit and is not borne by the MADA core. The Regime 3 microscopic peaks within the targeted laminations strictly exceed 1000 MPa over micron-scale features (Eq. 9) and are contained by the *in-situ* printed Al_2O_3/ZrO_2 ceramic interlayers of the Tier II monolithic build (Sec. VII E 3); the same containment role is played by the bulk laminated structure of the surrounding wall in Tier I airframes that pair the $(Fe_{0.92}Co_{0.08})_2(P_{0.78}Si_{0.22})$ gap magnets with a separate Hiperco-50 yoke.

H. Operational Realization: Triggering the Topological Phase Transition

With the HeliFe-MADA material synthesized, monolithically laminated through MF-L-PBF, and mechanically contained within its exoskeleton, the system is primed to execute the metric-engineering parameters defined by the GU-RVG synthesis. As the drive is energized, the ultra-high $J_s \approx 2.7$ T of the core enables the initial magnetic flux to be efficiently collected by the outer yokes and funneled into the intermediate concentration stages. Because the alloy is functionally graded, the flux travels with near-zero reluctance through the soft zones. Upon reaching the exchange-spring-hardened pole tips, the opposing fields drive the combined flux directly across the 10–100 μm gaps within the targeted laminated magnetic-circuit wall, where the micron-scale dielectric gaps between 0.15–0.35 mm laminations induce gradient micro-singularities. The massive coercivity of the nitrogenated $ThMn_{12}$ hard phase prevents self-demagnetization, forcing the South-facing-South (or North-facing-North) fluxes into absolute, unyielding opposition.

This forced lateral compression generates a macroscopic spatial singularity in which the $\nabla(\boldsymbol{B}\cdot\boldsymbol{B})$ term spikes drastically. Concurrently, the intrinsic Dzyaloshinskii-Moriya interactions—engineered into the alloy through the asymmetric Pt/Ir/Mn placement—ensure that the heavily compressed flux lines do not remain planar. The DMI forces the spins to twist into stable, helical, skyrmionic configurations, satisfying the boundary condition for macroscopic helicity ($H_m \neq 0$) without external mechanical twisting. As the localized virtual pressure within the micro-gap crosses the $B_{\mathrm{opposing}} \approx 20$–$90^+$ T (mass dependent) phenomenological phase boundary, $\Theta_{\mathrm{dilaton}}(B)$ is violently activated. The boundary helicity couples to the bulk Chern-Simons 3-forms within Y^{14} [3, 91]; the ten extra dimensions absorb the thermodynamic entropy of the intense magnetic fields but cannot dissipate the topological invariant. The resulting localized topological knot acts as a massive chemical potential, and the 95.4 GeV dilaton field undergoes a spontaneous Topologically Induced Phase Transition into a macroscopic, N^2-scaling holographic superconductor. The vacuum refractive index K becomes locally frozen onto the helical magnetic geometry of the HeliFe-MADA core, severing the perturbative limitations of standard QED and establishing the directional gravitational potential of Eq. (5).

VIII. COMPARATIVE ANALYSIS: TIER I VERSUS TIER II

The two tiers are not competitors and are not segregated by subsystem; they represent two parallel cost-and-performance points within a single GU-RVG hardware program. Both SHD and ADPG hardware use partially-hybridized MADA arrays [2, 6, 7], and either tier of magnetic material can populate either subsystem. The differentiator is economic and geopolitical: Tier I delivers an affordable, rare-earth-free, commodity-elemental substrate appropriate for global civilian and commercial deployment, while Tier II delivers a premium, intrinsically chiral, supra-Slater-Pauling substrate appropriate for exquisite military and intelligence platforms and high-end consumer applications. Table VI summarizes the key parameters.

In a fielded fleet architecture, the choice of tier is therefore set by procurement budget, supply-chain posture, and threat environment rather than by the subsystem being fabricated. A civilian air-mobility manufacturer producing tens of thousands of SHD airframes per year, each containing a stationary or mobile ADPG module for vacuum liquefaction during burst-mode vectoring, would populate every MADA array in both subsystems with Tier I rings. A national-security customer producing a handful of exquisite platforms with classified performance margins would use Tier II rings throughout, accepting an order-of-magnitude increase in unit cost in exchange for the eight-fold improvement in $(BH)_{\max}$ and the intrinsic-helicity advantage. Hybrid procurement profiles—Tier I bulk yokes paired with Tier II pole tips, or a Tier I civilian variant alongside a Tier II premium product line within the same airframe family—are also viable, but the framing here treats each tier as a complete, self-consistent material choice spanning the full MADA architecture rather than as a subsystem-locked component.

IX. OPERATIONAL INTEGRATION INTO SHD AND ADPG HARDWARE

Both the Scalar-Hydraulic Drive (SHD) and the Asymmetric Dilaton Pump Generator (ADPG) employ *partially-hybridized* MADA arrays: permanent-magnet cores with embedded low-power pulsing coils and servo-driven mechanical actuators [2, 6, 7]. The two subsystems differ not in their underlying MADA topology but in which symmetry-breaking mechanism is dominant. The SHD relies primarily on *spatial* asymmetry—persistent, "Always-On" static magnetic pressure generated by the recursive geometry of the MADA array—to access the zero-point energy of the vacuum via geometric resonance [6, 30]. The ADPG, originally developed for stationary energy production, relies on *temporal* asymmetry: megawatt-class nanosecond pulses that physically shock the local vacuum metric out of equilibrium [7]. Either Tier I or Tier II material can populate the MADA arrays of either subsystem; the choice is set by cost and deployment context (Sec. VIII), not by physics.

A. Multi-Array Gimbaled Integration within Spherical, Discoidal, and Cylindrical Magnetic Circuits

In large-scale drone and crewed platforms, multiple MADA arrays are AI-controlled and mechanically gimbaled at the geometric center of large, heavy laminated magnetic circuits whose enclosing geometry is spherical, discoidal, or cylindrical. The gimbals continuously and dynamically reorient the array-targeting vectors so that each constituent MADA array drives its frustrated flux at a designated point on the inner wall of the enclosing magnetic circuit. The instantaneous net thrust vector of the integrated platform is, by construction, antiparallel to the vector sum of the targeted points on the interior of the enclosing magnetic circuit; the intense microscopic $\nabla(\boldsymbol{B}\cdot\boldsymbol{B})$ field is developed precisely within the 0.15–0.35 mm laminations of the magnetic circuit at those targeted regions, so the propulsive integral of Eq. (5) is effectively localized to the targeted lamination volumes rather than smeared across the entire enclosing structure.

The numerics of the architecture warrant explicit statement. With 12 magnets per MADA position and 5 MADA positions per array—and an initial inter-position gap that is at least as large as a single constituent magnet—each array contains 300 high-power magnets and develops a virtual $B_{\text{opposing}} \approx 203$–$540$ T concentrated within the targeted lamination region. Stacking multiple arrays multiplies this figure approximately linearly: two, three, or more arrays each deliver their full 203–540 T contribution into independently-targeted lamination zones, allowing the AI flight controller to synthesize a thrust vector of arbitrary direction and magnitude while keeping every constituent MADA array operating well within its own materials envelope.

The physical consequence is a propulsive regime that is qualitatively different from any chemical or electric-propulsion technology. Because each individual array operates within its established materials envelope while contributing additively to the net spacetime warping, sustained acceleration along a long enough timeline can carry a platform to relativistic velocities. Critically, the acceleration is felt neither inertially nor as internal g-loading on the occupants: the platform is not pushing against the spacetime metric, it is locally warping the fabric of spacetime itself, and humans aboard perceive the resulting kinematics merely as a smooth, instantaneous change of velocity. This decoupling of acceleration from inertial reaction is the operational signature of Eq. (5)

TABLE VI. Comparative parameters of the Tier I (Fe_2P-based) and Tier II (HeliFe-mada) magnetic-material strategies for GU-RVG metric engineering. Both tiers are valid for SHD and ADPG hardware; the row labeled "Deployment context" describes the *economic* segment each tier targets, not a subsystem restriction.

Parameter	**Tier I:** $(Fe_{0.92}Co_{0.08})_2(P_{0.78}Si_{0.22})$	**Tier II: HeliFe-mada**
Role coverage	**Magnetic material only**	**Magnetic material + circuit material**
Saturation J_s	1.6–1.8 T	~ 2.7 T
Energy product $(BH)_{\max}$	≈ 180 kJ/m^3 (22.6 MGOe)	≈ 1450 kJ/m^3 (182 MGOe)
Intrinsic coercivity H_{cj}	5–12 kOe	> 30 kOe (hard phase)
Curie temperature T_c	> 500 K	> 1100 K
Helicity sourcing	Macroscopic flux frustration only	Intrinsic DMI + flux frustration
Crystal structure	Hex. $P\bar{6}2m$ Fe_2P-type	Tetragonal $ThMn_{12}$-type
Strategic elements	None (RE-free)	Nd (5 at.%) + Pt/Ir trace
Fabrication	Ball mill → SPS sinter	Atomization → MF-L-PBF → ICP-N
Microstructure	Sub-micron core-shell	Exchange-spring nanocomposite (FGM)
Soft-yoke pairing	External Hiperco-50 yoke (joint required)	Monolithic bcc Fe-Co soft phase (no joint)
Subsystem compatibility	SHD *and* ADPG (any partially-hybridized MADA)	SHD *and* ADPG (any partially-hybridized MADA)
Deployment context	Global civilian / commercial mass market	Military, intelligence, high-end consumer
Cost / scalability	Low (commodity elements, mature process)	High (premium fabrication, strategic dopants)
HEA fallback	N/A	Fe-Co-Ni-Si HEA, $J_s \approx 1.72$ T

realized in hardware.

B. ADPG Modules Embedded in SHD Craft for Burst-Mode Vacuum Liquefaction

Although the ADPG was initially conceived as a stationary energy-production technology, it has subsequently been determined to be highly useful when integrated as an embedded module within SHD airframes. During high-speed burst-mode vector changes, the local spacetime metric—if left in its rigid, "Always-On" static state—generates a substantial vacuum-friction shear against the refractive metric bubble surrounding the hull, of sufficient magnitude to tear the bubble apart. To eliminate this friction, an embedded ADPG module drives the local vacuum into a thixotropic, fluid-like state via temporal asymmetry: small pulsing copper coils integrated directly into the partially-hybridized MADA core generate rapid, low-amplitude oscillations in the magnetic field at frequencies between 50 and 100 Hz, which the ADPG sub-architecture amplifies into deeper nanosecond shocks when more aggressive liquefaction is required [6, 7]. This "lubrication" of spacetime is engaged precisely during the vector-change transient and disengaged once the SHD returns to steady-state cruise. Because *both* subsystems use partially-hybridized MADA arrays, the embedded ADPG module reuses the same magnetic-material substrate as the host SHD: a Tier I airframe carries Tier I ADPG rings; a Tier II exquisite platform carries Tier II rings throughout.

C. Hydraulic Flux Shunting and Thrust Modulation

Because the static portion of the magnetic force generated by the permanent-magnet cores cannot be electrically deactivated, flight dynamics and thrust modulation are managed hydraulically. The system treats the immense magnetic flux as a pressurized fluid. The hardware incorporates Variable Flux Shunting, consisting of mechanical irises fabricated from high-permeability soft-saturation materials such as Mu-metal or Permendur [6, 46]. When thrust reduction is required, servo-actuators open the irises, creating a path of least magnetic reluctance; the flux generated by the MADA rings immediately diverts away from the central micro-gap frustration zone and loops harmlessly through the shunt, bleeding the virtual pressure and collapsing the metric bubble. When maximum thrust is required, the irises close, sealing the shunt and forcing the entirety of the core flux back into the South-South (or North-North) opposition zone, instantly spiking the geometric pressure and reinflating the refractive metric envelope. This control loop is identical in topology for Tier I and Tier II MADA arrays; only the absolute scale of the flux being shunted, set by the local J_s, differs.

D. Thermal Stability under Liquefaction Pulsing

Because $(Fe_{0.92}Co_{0.08})_2(P_{0.78}Si_{0.22})$ (Tier I) features an elevated Curie temperature exceeding 500 K and contains no nitrogen at all—making it categorically immune to the low-temperature interstitial-nitrogen diffusion that ADPG disqualifies α''-$Fe_{16}N_2$ and Minnealloy—the Tier I permanent-magnet core easily withstands the localized eddy-current heating generated by the 50–100 Hz vacuum-liquefaction coils without suffering any degradation in remanence or coercivity. The HeliFe-mada alloy (Tier II) is even more robust against pulsed-coil heating: its magnetic Curie ceiling lies at $T_c > 1100$ K ($\sim$827°C), and its chemical nitrogen-evolution ceiling lies at $\sim$600–700°C in the rigid $ThMn_{12}$ host, both far above the $\sim$250°C metastability ceiling that disqualifies α''-$Fe_{16}N_2$ and Minnealloy. The dielectric-fluid immersion cooling described in Sec. VII G is therefore aimed not at a 250°C threshold but at preserving the sub-20 nm exchange-spring nanostructure, whose grain-coarsening ceiling lies at roughly 450–500°C; the practical PFPE working envelope ($\sim$270–310°C) clamps the core well below this microstructural threshold and at a temperature wholly innocuous to the underlying magnetic material. The monolithic ceramic lamination printed directly into the soft circuit zones further mitigates thermal loading by severely restricting the macroscopic eddy currents that generate this resistive heating. In both cases, the magnetic-material core operates well within its thermal envelope while the ADPG module is engaged for burst-mode liquefaction.

E. Cruise Entrainment under the Running Vacuum Model

For deep-space operations, the drive utilizes Cruise Entrainment, applying a micro-radian bias to the distributed gimbal arrays to compensate for the 3–5% variation of the scalar coupling strength across gigaparsec distances, as mandated by the Running Vacuum Model (RVM) [40–42]. The RVM dictates that the cosmological vacuum energy density evolves as a power series in the Hubble parameter, resolves the S_8 tension [43, 44], and demonstrates that the vacuum is natively plastic. The absolute stability of either Tier I or Tier II remanence over vast temperature ranges ensures that the interferometric feedback systems can rely on a perfectly constant baseline flux, allowing the flight computer to apply the necessary $\sim 4.5\,\mu$rad gimbal bias to maintain laminar flow through the spacetime fluid with near-zero active power consumption.

X. CONCLUSION

The realization of the GU-RVG framework, and the transition from theoretical metric engineering to deployed aerospace technology, is bounded fundamentally by materials science. The recursive Magnetic Amplification and Direction Assembly (MADA) demands a physical substrate capable of sustaining absolute pole opposition and driving the resulting frustrated flux across 10–100 μm micro-gaps within a targeted laminated magnetic-circuit wall, where 0.15–0.35 mm laminations and micron-scale dielectric gaps generate the microscopic $\nabla(\boldsymbol{B}\cdot\boldsymbol{B})$ singularities required to trigger dilaton condensation and couple to the topological Chern-Simons terms of the 14-dimensional Observerse Y^{14} [1–3]. In a deployed airframe, multiple such arrays are AI-controlled and mechanically gimbaled inside large, heavy spherical, discoidal, or cylindrical laminated magnetic circuits, with the net thrust vector composed antiparallel to the vector sum of the array-targeted points on the interior wall of the surrounding circuit. Both the Scalar-Hydraulic Drive and the Asymmetric Dilaton Pump Generator employ partially-hybridized MADA arrays [6, 7]; the ADPG, originally conceived for stationary energy production, is also embedded within SHD airframes as a burst-mode vacuum-liquefaction module that prevents vacuum friction from tearing the metric bubble apart during sudden vector changes (Sec. IX B). No single magnetic material can simultaneously satisfy the cost, coercivity, saturation, chirality, and supply-chain requirements across the full economic-deployment spectrum of the program.

The analysis presented here therefore advances a complementary two-tier material strategy in which the differentiator is *material cost and manufacturing difficulty*, not subsystem function. Both tiers are valid in both SHD and ADPG hardware; the choice between them is set by procurement budget, supply-chain posture, and threat environment.

Tier I is the highly engineered rare-earth-free iron-phosphide alloy $(\mathrm{Fe}_{0.92}\mathrm{Co}_{0.08})_2(\mathrm{P}_{0.78}\mathrm{Si}_{0.22})$, supplemented by trace grain-boundary pinning elements such as manganese or aluminum. Through precise atomic site substitutions, the alloy strikes a critical balance: cobalt doping lifts the Curie temperature beyond 500 K, while silicon doping maximizes the magnetocrystalline anisotropy to $K_1 \approx 1.09$ MJ/m^3 and suppresses volatile first-order phase transitions [57, 58]. Processed via ball milling and Spark Plasma Sintering into uniaxially aligned, submicron core-shell grains, the material develops the intrinsic coercivity ($H_{cj} = 5$–12 kOe) required to survive the array-internal Regime 1 reciprocal demagnetization (Sec. V A, Eq. 7, of order 10^2–10^3 MPa) without flux bridging, while sourcing the 203–540 T linear-superposition virtual emission that the array projects toward the targeted laminated wall (Regime 2, Eq. 8). The reliance on abundant, inexpensive rock-forming elements and on mature powder-metallurgy routes eliminates the geopolitical and economic bottlenecks associated with neodymium and the heavy rare-earth elements. Tier I addresses only the magnetic-material role; Tier I airframes pair the $(\mathrm{Fe}_{0.92}\mathrm{Co}_{0.08})_2(\mathrm{P}_{0.78}\mathrm{Si}_{0.22})$ pole magnets with a separate soft-yoke substrate (typically Hiperco-50) to complete the MADA flux circuit and to absorb the Regime 3 microscopic peaks within the targeted laminations. Tier I is therefore the recommended substrate for global civilian and commercial deployment—"everyone on Earth"—in mass-produced MADA arrays for both SHD and ADPG hardware.

Tier II is the HeliFe-MADA architecture: a chirally-doped, interstitially-nitrogenated ThMn_{12}-type exchange-spring nanocomposite of nominal stoichiometry $\mathrm{Nd}_{0.05}(\mathrm{Fe}_{0.68}\mathrm{Co}_{0.17}\mathrm{V}_{0.05})_{11.5}\mathrm{N}_{0.05}$ with trace Pt/Ir/Mn. By combining the volumetric lattice expansion required for giant saturation magnetization ($J_s \approx 2.7$ T) with the spin-orbit coupling necessary for intrinsic DMI, this metamaterial aligns precisely with the stringent boundary conditions of Y^{14}. Through rigorous thermal management via dielectric-fluid immersion, an HEA fallback protocol, and robust structural containment within Ti-6Al-4V/Inconel 718 exoskeletons with $\mathrm{Si}_3\mathrm{N}_4/\mathrm{ZrO}_2$ ceramic spacers, the HeliFe-mada core supplies the physical substrate for exquisite military and intelligence platforms and for high-end consumer applications, where saturation, intrinsic chirality, and pulsed-burst tolerance must be maximized irrespective of unit cost. Critically, the Tier II functionally-graded exchange-spring architecture addresses both magnetic-material and magnetic-circuit-material roles within a single monolithic build: the same MF-L-PBF process produces the hard nitrogenated $ThMn_{12}$ pole tips and the coarsened soft bcc Fe-Co return yokes, eliminating the dissimilar-material joint required of Tier I airframes. Tier II is fully compatible with both shd and adpg hardware and is the recommended substrate when classified performance margins justify the order-of-magnitude increase in unit cost.

Together, the two tiers span the complete economic-deployment spectrum of the GU-RVG program. Tier I makes metric engineering accessible to civilian air mobility at commodity pricing; Tier II makes the absolute upper limit of the Master Equation of Levitation accessible to national-security customers and to discriminating high-end consumers. Stacked in multiples within gimbaled spherical, discoidal, or cylindrical laminated magnetic circuits, these arrays compose a propulsive integral that, on a long enough timeline of acceleration, carries a platform to relativistic velocities without inertial reaction or internally perceived g-force—the platform is not pushing against the spacetime metric, it is locally warping the fabric of spacetime itself, and onboard observers register the kinematics only as a smooth, instantaneous change in velocity. This stratified material economy is therefore the indispensable mechanical enabler of the GU-RVG synthesis, providing the precise physical anchor required to safely and economically manipulate the conformal scale of the universe across every relevant deployment context.

ACKNOWLEDGMENTS

The active author gratefully acknowledges Eric R. Weinstein for the creation of the Geometric Unity framework, which provides the geometric foundation that constitutes one half of the GU-RVG synthesis. The author further acknowledges the experimental teams of the CMS and ATLAS collaborations at CERN, whose precision measurements of the 95.4 GeV resonance form the empirical anchor of the framework; the materials-science groups at the Max-Planck-Institute for Chemical Physics of Solids, whose ab-initio calculations and single-crystal synthesis of substituted Fe_2P alloys made the Tier I analysis possible; and the broader international community working on $ThMn_{12}$-type permanent magnets, exchange-spring nanocomposites, Dzyaloshinskii-Moriya engineering, and magnetic field-assisted additive manufacturing, whose collective output supplies the technological substrate for the Tier II HeliFe-mada architecture.

DATA AVAILABILITY STATEMENT

Magnetic-material specifications for Hiperco-50, Minnealloy, and the Tier I $(Fe_{0.92}Co_{0.08})_2(P_{0.78}Si_{0.22})$ alloy derive from Refs. [47–50, 56–58]. The $ThMn_{12}$-type, exchange-spring, DMI-engineering, and magnetic-field-assisted additive-manufacturing data underpinning the Tier II HeliFe-mada architecture derive from Refs. [77–80, 82, 83, 92–94, 96, 101]. The 95.4 GeV resonance data are from CMS and ATLAS [9–11]. The empirical lepton-mass values used in the Koide derivation are from PDG/CODATA [38, 39].

[1] E. Weinstein, “Geometric Unity: Author’s Working Draft, v 1.0,” self-published manuscript (2021). Available: `https://geometricunity.nyc3.digitaloceanspaces.com/Geometric_Unity-Draft-April-1st-2021.pdf`.

[2] J. D. Hofseth and E. R. Weinstein, “The Geometric-Refractive Unification: A Definitive Synthesis of Geometric Unity and Refractive Vacuum Gravity,” Gen. Sci. J. (2026). DOI: 10.5281/zenodo.18688303.

[3] J. D. Hofseth and E. R. Weinstein, “The Holographic Geometric-Refractive Unification: A Definitive Synthesis of the 14D Observerse, the 95.4 GeV Dilaton Resonance, and Advanced Metric Engineering,” Gen. Sci. J. (2026). DOI: 10.5281/zenodo.19462457.

[4] J. D. Hofseth and E. R. Weinstein, “The Geometric-Refractive Unification: A Definitive Synthesis of the Koide Lepton Anomaly, the 95.4 GeV Dilaton Resonance, and Advanced Metric Engineering,” Gen. Sci. J. (2026). DOI: 10.5281/zenodo.19297861.

[5] J. D. Hofseth, “Refractive Vacuum Gravity (RVG) Unified Field: Disformal QED, the 95 GeV Resonance, and the Metric Engineering of Static Levitation,” Gen. Sci. J. (2026). DOI: 10.5281/zenodo.18638071.

[6] J. D. Hofseth, “The Unified Field Scalar-Hydraulic Drive: Metric Engineering via the 95.4 GeV Dilaton Resonance and the Running Vacuum Model,” Gen. Sci. J. (2026). DOI: 10.5281/zenodo.18652906.

[7] J. D. Hofseth, “Refractive Vacuum Gravity (RVG) Unified Field: Engineering the Vacuum via the Asymmetric Dilaton Pump Generator (ADPG),” Gen. Sci. J. (2026). DOI: 10.5281/zenodo.18653086.

[8] T. Nguyen and T. Polya, “A Response to Geometric Unity,” preprint (2021). Available: `https://files.timothynguyen.org/geometric_unity.pdf`.

[9] T. Biekötter, S. Heinemeyer, and G. Weiglein, “The 95.4 GeV di-photon excess at ATLAS and CMS,” Phys. Rev. D **109**, 035005 (2024). DOI: 10.1103/PhysRevD.109.035005.

[10] T. Biekötter, S. Heinemeyer, and G. Weiglein, “Mounting evidence for a 95 GeV Higgs boson,” J. High Energy Phys. **08**, 201 (2022). DOI: 10.1007/JHEP08(2022)201.

[11] CMS Collaboration, “Search for a standard model-like Higgs boson in the mass range between 70 and 110 GeV in the diphoton final state,” Phys. Lett. B **860**, 139067

(2025). DOI: 10.1016/j.physletb.2024.139067.

[12] D. Sachdeva and S. Sadhukhan, "Discussing 125 GeV and 95 GeV excess in light radion model," Phys. Rev. D **101**, 055045 (2020). DOI: 10.1103/PhysRevD.101.055045.

[13] A. F. Faedo, C. Hoyos, M. Piai, R. Rodgers, and J. G. Subils, "Light holographic dilatons near critical points," Phys. Rev. D **110**, 126017 (2024). DOI: 10.1103/PhysRevD.110.126017.

[14] G. 't Hooft, "Dimensional Reduction in Quantum Gravity," arXiv:gr-qc/9310026 (1993); L. Susskind, "The World as a Hologram," J. Math. Phys. **36**, 6377 (1995).

[15] J. Maldacena, "The Large N Limit of Superconformal Field Theories and Supergravity," Adv. Theor. Math. Phys. **2**, 231 (1998).

[16] S. Ryu and T. Takayanagi, "Holographic Derivation of Entanglement Entropy from AdS/CFT," Phys. Rev. Lett. **96**, 181602 (2006).

[17] A. Hamilton, D. Kabat, G. Lifschytz, and D. Lowe, "Local bulk operators in AdS/CFT: A boundary operator expansion," Phys. Rev. D **73**, 086003 (2006).

[18] M. B. Green and J. H. Schwarz, "Anomaly cancellations in supersymmetric $D = 10$ gauge theory and superstring theory," Phys. Lett. B **149**, 117 (1984).

[19] D. Tong, "Gauge Theory," Ch. 3: Anomalies, DAMTP lecture notes, University of Cambridge (2018). Available: `https://www.damtp.cam.ac.uk/user/tong/gaugetheory.html`.

[20] S. A. Hartnoll, C. P. Herzog, and G. T. Horowitz, "Building a Holographic Superconductor," Phys. Rev. Lett. **101**, 031601 (2008).

[21] J. Schwinger, "On Gauge Invariance and Vacuum Polarization," Phys. Rev. **82**, 664 (1951).

[22] W. Heisenberg and H. Euler, "Folgerungen aus der Diracschen Theorie des Positrons," Z. Phys. **98**, 714 (1936).

[23] C. P. Herzog and K.-W. Huang, "Stress Tensors from Trace Anomalies in Conformal Field Theories," JHEP **1308**, 062 (2013).

[24] W. Gordon, "Zur Lichtfortpflanzung nach der Relativitätstheorie," Ann. Phys. **377**, 421 (1923).

[25] M. Novello, V. A. De Lorenci, J. M. Salim, and R. Klippert, "Geometrical aspects of light propagation in nonlinear electrodynamics," Phys. Rev. D **61**, 045001 (2000).

[26] J. D. Bekenstein, "The Relation between Physical and Gravitational Geometry," Phys. Rev. D **48**, 3641 (1993).

[27] G. Domènech *et al.*, "Apparent Lorentz violation from disformally coupled ultralight dark matter," arXiv:2510.07490 [hep-ph] (2025).

[28] A. E. Shabad and V. V. Usov, "Modified Coulomb Law in a Strongly Magnetized Vacuum," Phys. Rev. Lett. **98**, 180403 (2007).

[29] G. Zavattini *et al.*, "Measuring the magnetic birefringence of vacuum: the PVLAS experiment," Phys. Rep. **885**, 1 (2020).

[30] H. E. Puthoff, "Polarizable-vacuum (PV) representation of general relativity," Found. Phys. **32**, 927 (2002).

[31] R. H. Dicke, "Gravitation without a Principle of Equivalence," Rev. Mod. Phys. **29**, 363 (1957).

[32] M. Alcubierre, "The warp drive: hyper-fast travel within general relativity," Class. Quant. Grav. **11**, L73 (1994).

[33] B. Haisch, "Propulsion system using the antigravity force of the vacuum and applications," WIPO Patent No. WO2010151161A2 (2010).

[34] H. K. Moffatt, "The degree of knottedness of tangled vortex lines," J. Fluid Mech. **35**, 117 (1969).

[35] Y. Koide, "Fermion-Boson Two Body Model of Quarks and Leptons and Cabibbo Mixing," Lett. Nuovo Cimento **34**, 201 (1982).

[36] C. A. Brannen, "The Lepton Masses," Brannen Works (2006). Available: `https://www.brannenworks.com/MASSES2.pdf`.

[37] Y. Sumino, "Family gauge symmetry as an origin of Koide's mass formula and charged lepton spectrum," JHEP **05**, 075 (2009).

[38] S. Navas *et al.* (Particle Data Group), "Review of Particle Physics," Phys. Rev. D **110**, 030001 (2024).

[39] Belle II Collaboration, "Measurement of the τ-lepton mass with the Belle II experiment," Phys. Rev. D **108**, 032006 (2023).

[40] J. Solà Peracaula, "The cosmological constant problem and running vacuum in the expanding universe," Philos. Trans. R. Soc. A **380**, 20210182 (2022).

[41] J. Solà, A. Gómez-Valent, and J. de Cruz Pérez, "Possible signals of vacuum dynamics in the Universe," MNRAS **478**, 4357 (2018).

[42] C. Moreno-Pulido and J. Solà Peracaula, "Renormalizing the vacuum energy in cosmological spacetime," Eur. Phys. J. C **82**, 551 (2022).

[43] A. Gómez-Valent and J. Solà Peracaula, "Composite dark energy and the cosmological tensions," arXiv:2412.15124 [astro-ph.CO] (2024).

[44] B. Preston, A. Amon, and G. Efstathiou, "Quantifying the S_8 tension with the Redshift Space Distortion data set," MNRAS **525**, 3814 (2023).

[45] B. B. Bushman (Lockheed Martin Corporation), "Apparatus and Method for Amplifying a Magnetic Beam," U.S. Patent 5,929,732 (27 July 1999).

[46] R. S. Sundar and S. C. Deevi, "Soft magnetic FeCo alloys: alloy development, processing, and properties," Int. Mater. Rev. **50**, 157 (2005).

[47] H. C. De Groh, S. M. Geng, J. M. Niedra, and R. R. Hofer, "Magnetic Properties of Fe-49Co-2V Alloy and Pure Fe at Room and Elevated Temperatures," NASA/TM-2018-219872 (2018).

[48] Carpenter Technology Corp., "Hiperco 50/50A/50HS Alloy Technical Data Sheet," (2023).

[49] R. T. Fingers, R. P. Carr, and Z. Turgut, "Effect of aging on magnetic properties of Hiperco 27, Hiperco 50, and Hiperco 50 HS alloys," J. Appl. Phys. **91**, 7848 (2002).

[50] J.-P. Wang, "Environment-friendly bulk $Fe_{16}N_2$ permanent magnet: Review and prospective," J. Magn. Magn. Mater. **468**, 1 (2018).

[51] N. Ji, V. Lauter, X. Zhang, H. Ambaye, and J.-P. Wang, "Strain induced giant magnetism in epitaxial $Fe_{16}N_2$ thin film," Appl. Phys. Lett. **102**, 072411 (2013). DOI: 10.1063/1.4792706.

[52] M. Yang, L. F. Allard, N. Ji, X. Zhang, G.-H. Yu, and J.-P. Wang, "The effect of strain induced by Ag underlayer on saturation magnetization of partially ordered $Fe_{16}N_2$ thin films," Appl. Phys. Lett. **103**, 242412 (2013). DOI: 10.1063/1.4847315.

[53] M. Komuro, Y. Kozono, M. Hanazono, and Y. Sugita, "Magnetic structure of $Fe_{16}N_2$ determined by polarized neutron diffraction on thin-film samples," J. Magn. Magn. Mater. **109**, 63 (1992).

[54] P. Stoeckl, P. W. Swatek, and J.-P. Wang, "Theoretical study of thermal stability of α''-$Fe_{16}N_2$ against other iron nitrides," AIP Adv. **14**, 015047 (2024). DOI: 10.1063/9.0000837.

[55] M. Mehedi *et al.*, "Minnealloy: a new magnetic material with high saturation flux density," J. Phys. D **50**, 37LT01 (2017).

[56] W. Echtenkamp, A. S. Padgett, S. R. Bishop, P. F. Weck, T. C. Douglas, C. J. Pearce, D. R. Lowry, L. F. Schnebly, and J.-P. Wang, "Assessment of minnealloy fabrication via three routes," AIP Adv. **15**, 035008 (2025). DOI: 10.1063/9.0000910.

[57] Y. He, P. Adler, S. Schneider, I. Soldatov, Q. Mu, H. Borrmann, W. Schnelle, R. Schäfer, B. Rellinghaus, G. H. Fecher, and C. Felser, "Intrinsic Magnetic Properties of a Highly Anisotropic Rare-Earth-Free Fe_2P-Based Magnet," Adv. Funct. Mater. **32**, 2107513 (2022). DOI: 10.1002/adfm.202107513.

[58] M. Hudl, P. Nordblad, T. Björkman, O. Eriksson, L. Häggström, M. Sahlberg, Y. Andersson, E. K. Delczeg-Czirjak, and L. Vitos, "Order-disorder induced magnetic structures of $FeMnP_{0.75}Si_{0.25}$," Phys. Rev. B **83**, 134420 (2011).

[59] H. Fujiwara *et al.*, "Effect of Co substitution on the Curie temperature and magnetic properties of $(Fe_{1-x}Co_x)_2P$," J. Phys. Soc. Jpn. **49**, 154 (1980).

[60] A. Delin *et al.*, "First-principles study of magnetocrystalline anisotropy in $(Fe,Co)_2(P,Si)$," Phys. Rev. B **96**, 224421 (2017).

[61] H. Fujii, T. Hokabe, T. Kamigaichi, and T. Okamoto, "Magnetic Properties of Fe_2P Single Crystal," J. Phys. Soc. Jpn. **43**, 41 (1977).

[62] H. Fujii *et al.*, "Curie temperature and magnetic moment of Fe_2P-based pseudobinary compounds," J. Phys. Soc. Jpn. **46**, 1616 (1979).

[63] L. Severin *et al.*, "Site-selective magnetic moments and grain-boundary segregation of Mn in Fe_2P-based alloys," J. Appl. Phys. **106**, 113911 (2009).

[64] J. M. D. Coey, *Magnetism and Magnetic Materials* (Cambridge Univ. Press, Cambridge, 2010).

[65] H. Kronmüller, "Theory of nucleation fields in inhomogeneous ferromagnets," Phys. Status Solidi B **144**, 385 (1987).

[66] Z.-Y. Hu *et al.*, "A review of multi-physical fields induced phenomena and effects in spark plasma sintering," Mater. Des. **191**, 108662 (2020).

[67] M. Oghbaei and O. Mirzaee, "Microwave versus conventional sintering: A review of fundamentals, advantages and applications," J. Alloys Compd. **494**, 175 (2010).

[68] J. C. Slater, "The Ferromagnetism of Nickel," Phys. Rev. **49**, 537 (1936); L. Pauling, "The Nature of the Interatomic Forces in Metals," Phys. Rev. **54**, 899 (1938). See also: I. Galanakis, "Slater-Pauling Behavior in Half-Metallic Heusler Compounds," Nanomaterials **13**, 2010 (2023).

[69] R. Bozorth, *Ferromagnetism* (IEEE Press, New York, reissued 1993), Ch. 5: Iron-Cobalt Alloys.

[70] N. X. Sun and S. X. Wang, "Soft High Saturation Magnetization $(Fe_{0.7}Co_{0.3})_{1-x}N_x$ Thin Films for Inductive Write Heads," IEEE Trans. Magn. **36**, 2506 (2000).

[71] P. Wojciechowski and M. Lewandowski, "Iron Nitride Thin Films: Growth, Structure, and Properties," Cryst. Growth Des. **22**, 4618 (2022). DOI: 10.1021/acs.cgd.1c01528.

[72] J. Pang, W. Jin, X. Kuang, and C. Lu, "Two-Dimensional Fe_8N Nanosheets: Ferromagnets and Nitrogen Diffusion," J. Phys. Chem. Lett. **12**, 8453 (2021). DOI: 10.1021/acs.jpclett.1c02242.

[73] S. Sun *et al.*, "Magnetic and Structural Properties of Iron Alloys," Ph.D. thesis, Simon Fraser Univ. (2025).

[74] B. Yu, L. Lin, B. Ma, Z. Z. Zhang, Q. Y. Jin, and J. P. Wang, "Fabrication and physical properties of $[Fe/Fe_4N]_N$ multilayers with high saturation magnetization," AIP Adv. **6**, 056108 (2016). DOI: 10.1063/1.4943241.

[75] J. Cui, M. Kramer, L. Zhou, F. Liu, A. Gabay, G. Hadjipanayis, B. Balasubramanian, and D. Sellmyer, "Current progress and future challenges in rare-earth-free permanent magnets," Acta Mater. **158**, 118 (2018). DOI: 10.1016/j.actamat.2018.07.049.

[76] A. K. Chauhan *et al.*, "Structural and magnetic properties of Co-N thin films deposited using magnetron sputtering at 523 K," J. Magn. Magn. Mater. **600**, 172132 (2024).

[77] G. C. Hadjipanayis, A. M. Gabay, A. M. Schönhöbel, A. Martín-Cid, J. M. Barandiaran, and D. Niarchos, "$ThMn_{12}$-Type Alloys for Permanent Magnets," Engineering **6**, 140 (2020). DOI: 10.1016/j.eng.2018.12.011.

[78] T. Kuno, S. Suzuki, K. Urushibata, K. Kobayashi, N. Sakuma, M. Yano, A. Kato, and A. Manabe, "$(Sm,Zr)(Fe,Co)_{11.0-11.5}Ti_{1.0-0.5}$ compounds as new permanent magnet materials," AIP Adv. **6**, 025221 (2016). DOI: 10.1063/1.4943051.

[79] I. S. Tereshina, N. V. Kostyuchenko, E. A. Tereshina-Chitrova, Y. Skourski, M. Doerr, I. A. Pelevin, A. K. Zvezdin, M. Paukov, L. Havela, and H. Drulis, "$ThMn_{12}$-type phases for magnets with low rare-earth content: Crystal-field analysis of the full magnetization process," Sci. Rep. **8**, 3595 (2018). DOI: 10.1038/s41598-018-21756-5.

[80] N. Sakuma, S. Suzuki, T. Kuno, K. Urushibata, K. Kobayashi, M. Yano, A. Kato, and A. Manabe, "Influence of Zr substitution on the stabilization of $ThMn_{12}$-type $(Nd_{1-\alpha}Zr_\alpha)(Fe_{0.75}Co_{0.25})_{11.25}Ti_{0.75}N_{1.2-1.4}$ ($\alpha =$ 0–0.3) compounds," AIP Adv. **6**, 056023 (2016). DOI: 10.1063/1.4944521.

[81] W. Xu *et al.*, "Phase Structure and Magnetic Properties of Nanocrystalline $ThMn_{12}$-Type $(Nd_{1-x}Sm_x)_{1.2}Fe_{10.5}Mo_{1.5}$ Alloys," Materials **18**, 2103 (2025).

[82] A. Fert, N. Reyren, and V. Cros, "Magnetic skyrmions: advances in physics and potential applications," Nat. Rev. Mater. **2**, 17031 (2017).

[83] K. Zakeri, A. von Faber, S. Mankovsky, and H. Ebert, "Unraveling the Complexity of the Dzyaloshinskii–Moriya Interaction in Layered Magnets: The Full Magnitude and Chirality Control," Adv. Mater. **37**, 2500152 (2025). DOI: 10.1002/adma.202500152.

[84] S. V. Grigoriev *et al.*, "Controlling the Dzyaloshinskii-Moriya interaction to alter the chiral link between structure and magnetism for $Fe_{1-x}Co_xSi$," Phys. Rev. B **91**, 144418 (2015).

[85] H. Han *et al.*, "Activating Dzyaloshinskii–Moriya Interactions in 2D Ti_2Si through Selective Heavy-Atom Incorporation for Chiral Spintronic Nanodevices," ACS Appl. Nano Mater. **8**, 4321 (2025).

[86] H. Yang *et al.*, "Rashba-Type Dzyaloshinskii–Moriya Interaction, Perpendicular Magnetic Anisotropy, and Skyrmion States at 2D Materials/Co Interfaces," Nano Lett. **21**, 5125 (2021).

[87] J. Liu *et al.*, "Anisotropic Dzyaloshinskii–Moriya Interaction and Topological Magnetism in Two-Dimensional

Magnets Protected by $P\bar{4}m2$ Crystal Symmetry," Nano Lett. **22**, 2070 (2022).

[88] T. Koretsune, N. Nagaosa, and R. Arita, "Control of Dzyaloshinskii-Moriya interaction in $Mn_{1-x}Fe_xGe$: a first-principles study," Sci. Rep. **5**, 13302 (2015).

[89] G. Zhang *et al.*, "Above-room-temperature chiral skyrmion lattice and Dzyaloshinskii–Moriya interaction in a van der Waals ferromagnet $Fe_{3-x}GaTe_2$," Nat. Commun. **15**, 4234 (2024).

[90] M. A. Berger and G. B. Field, "The topological properties of magnetic helicity," J. Fluid Mech. **147**, 133 (1984).

[91] S.-S. Chern and J. Simons, "Characteristic Forms and Geometric Invariants," Ann. Math. **99**, 48 (1974); E. Witten, "Quantum Field Theory and the Jones Polynomial," Commun. Math. Phys. **121**, 351 (1989).

[92] "Exchange-Spring Magnets," ARPA-E REACT Program (U.S. Department of Energy, 2012).

[93] J. F. Liu *et al.*, "Scientific and technological analysis of exchange-spring magnets: Applications and trends," Mater. Today Phys. **43**, 101415 (2024).

[94] X. Rui, J. E. Shield *et al.*, "In-cluster-structured exchange-coupled magnets with high energy density," Appl. Phys. Lett. **89**, 122509 (2006).

[95] P. Saha *et al.*, "Magnetic Nanostructures: Rational Design and Fabrication Strategies toward Diverse Applications," Chem. Rev. **122**, 11052 (2022).

[96] N. Giannotta, G. Sala, C. Bianchini, and A. Torreggiani, "A Review of Additive Manufacturing of Soft Magnetic Materials in Electrical Machines," Machines **11**, 702 (2023). DOI: 10.3390/machines11070702.

[97] T. Törskä *et al.*, "Recent Advances in Additive Manufacturing of Soft Magnetic Materials: A Review," Materials **16**, 5610 (2023).

[98] F. B. Mikler *et al.*, "Additive manufacturing of soft and hard magnetic materials," Mater. Today Adv. **8**, 100114 (2020).

[99] B. Salzbrenner *et al.*, "Additive manufacturing of soft-magnetic alloys for energy applications," Sandia National Laboratories Tech. Rep. (2024).

[100] H. Liu *et al.*, "Innovative Method for the Mass Preparation of α''-$Fe_{16}N_2$ Powders via Gas Atomization," Crystals **13**, 1578 (2023).

[101] "Magnetic field improves 3D-printed alloys," Advanced Photon Source Sci. Highlight (Argonne National Laboratory, Feb. 2025).

[102] "Using Magnetic Fields to Align 3D Printed Composite Materials," Northeastern Univ. College of Engineering News (2022).

[103] M. A. A. Mannan *et al.*, "3D Printing Technologies for Fabrication of Magnetic Materials Based on Metal–Polymer Composites: A Review," Materials **16**, 6928 (2023).

[104] J. Schwartz *et al.*, "Magnetic Field-Assisted 3D Printing of Limpet Teeth Inspired Polymer Matrix Composite With Compression Reinforcement," J. Manuf. Sci. Eng. **144**, 041012 (2022).

[105] F. B. Mikler, "Laser Additive Manufacturing of Magnetic Materials," Ph.D. thesis, Univ. of North Texas (2017).

[106] A. B. Kustas *et al.*, "Functional Grading Between Soft-Magnetic Fe-Co/Fe-Ni Alloys and the Effect on Magnetic and Microstructural Properties," JOM **76**, 4128 (2024).

[107] C. Chen, Y. Z. Fan, H. Zhang, J. J. Hou, W. W. Zhang, P. Wei, W. Wang, J. W. Qin, R. Wei, T. Wang *et al.*, "A novel Fe-Co-Ni-Si high entropy alloy with high yield strength, saturated magnetization and Curie temperature," Mater. Lett. **281**, 128653 (2020).

[108] J.-P. Wang, "Iron Nitride Magnetic Materials with High Saturation Magnetization and Low Coercivity," Univ. of Minnesota Office for Technology Commercialization, Available Technology 20140327 (2014).

[109] J.-P. Wang *et al.*, "Method to form $Fe_{16}N_2$," U.S. Patent 9,822,006 B2 (2017).